Neurobiology of Disease

Disruption of Endosomal Sorting in Schwann Cells Leads to Defective Myelination and Endosomal Abnormalities Observed in Charcot-Marie-Tooth Disease

John W. McLean,[1] Julie A. Wilson,[1] Tina Tian,[1] Jennifer A. Watson,[1] Mary VanHart,[1] Andrew J. Bean,[3] Steven S. Scherer,[4] David K. Crossman,[5] Eroboghene Ubogu,[1,2] and Scott M. Wilson[1]

[1]Department of Neurobiology, Evelyn F. McKnight Brain Institute, Civitan International Research Center, University of Alabama at Birmingham, Birmingham, Alabama 35294, [2]Division of Neuromuscular Disease, Department of Neurology, University of Alabama at Birmingham, Birmingham, Alabama 35294, [3]Graduate College, Rush University, Chicago, Illinois 60612, [4]Department of Neurology, Perelman School of Medicine, University of Pennsylvania, Philadelphia, Pennsylvania 19104, and [5]Department of Genetics, University of Alabama at Birmingham, Birmingham, Alabama, 35294

Endosomal sorting plays a fundamental role in directing neural development. By altering the temporal and spatial distribution of membrane receptors, endosomes regulate signaling pathways that control the differentiation and function of neural cells. Several genes linked to inherited demyelinating peripheral neuropathies, known as Charcot-Marie-Tooth (CMT) disease, encode proteins that directly interact with components of the endosomal sorting complex required for transport (ESCRT). Our previous studies demonstrated that a point mutation in the ESCRT component hepatocyte growth-factor-regulated tyrosine kinase substrate (HGS), an endosomal scaffolding protein that identifies internalized cargo to be sorted by the endosome, causes a peripheral neuropathy in the neurodevelopmentally impaired *teetering* mice. Here, we constructed a Schwann cell-specific deletion of *Hgs* to determine the role of endosomal sorting during myelination. Inactivation of HGS in Schwann cells resulted in motor and sensory deficits, slowed nerve conduction velocities, delayed myelination and hypomyelinated axons, all of which occur in demyelinating forms of CMT. Consistent with a delay in Schwann cell maturation, HGS-deficient sciatic nerves displayed increased mRNA levels for several promyelinating genes and decreased mRNA levels for genes that serve as markers of myelinating Schwann cells. Loss of HGS also altered the abundance and activation of the ERBB2/3 receptors, which are essential for Schwann cell development. We therefore hypothesize that HGS plays a critical role in endosomal sorting of the ERBB2/3 receptors during Schwann cell maturation, which further implicates endosomal dysfunction in inherited peripheral neuropathies.

Key words: Charcot-Marie-Tooth; endosome; ESCRT; myelination; Schwann cell

Significance Statement

Schwann cells myelinate peripheral axons, and defects in Schwann cell function cause inherited demyelinating peripheral neuropathies known as CMT. Although many CMT-linked mutations are in genes that encode putative endosomal proteins, little is known about the requirements of endosomal sorting during myelination. In this study, we demonstrate that loss of HGS disrupts the endosomal sorting pathway in Schwann cells, resulting in hypomyelination, aberrant myelin sheaths, and impairment of the ERBB2/3 receptor pathway. These findings suggest that defective endosomal trafficking of internalized cell surface receptors may be a common mechanism contributing to demyelinating CMT.

Received Dec. 16, 2021; revised Apr. 24, 2022; accepted May 3, 2022.

Author contributions: J.W.M., S.S.S., E.U., D.K.C., and S.M.W. designed research; J.W.M., J.A.Wilson, T.T., J. A. Watson, M.V., D.K.C., E.U., and S.M.W., preformed research; A.J.B. contributed unpublished reagents/analytic tools; J.W.M., J.A.Wilson, T.T., J.A. Watson., M.V., S.S.S., D.K.C., E.U., and S.M.W. analyzed data; J.W.M., J.A.Wilson, A.J.B., S.S.S., E.U., and S.M.W. wrote the paper.

This research was supported by the University of Alabama at Birmingham Department of Neurobiology and the National Institute of Neurological Disorders and Stroke Grant NS110744 to S.M.W. We thank Edward Phillips at the University of Alabama Electron Microscopy Core for help with tissue processing and collection of sciatic nerve micrographs.

The authors declare no competing financial interests

Correspondence should be addressed to Scott M. Wilson at livvy01@uab.edu.

https://doi.org/10.1523/JNEUROSCI.2481-21.2022

Introduction

The endocytic pathway consists of a series of membrane trafficking steps that regulate the internalization of cell-surface receptors and lipids (Jovic et al., 2010; McNally and Cullen, 2018). Internalized cargo is initially delivered to early endosomes, where it is sorted into distinct endocytic routes (Naslavsky and Caplan, 2018). From here, internalized receptors can be recycled back to the cell surface through recycling endosomes, continue to activate signaling pathways while residing on early endosomes, or be sorted to late endosomes and subsequently to lysosomes, for degradation (Goh and Sorkin, 2013; Cullen and Steinberg, 2018). By

controlling the trafficking of internalized cell surface receptors in this spatial and temporal manner, the endosomal pathway regulates the composition, distribution, and density of receptors at the cell surface as well as the fate of signaling complexes within the cell (Redpath et al., 2020).

The endosomal sorting complex required for transport (ESCRT) pathway aids in sequestering internalized cell surface cargo on the endosome and determines how it is directed along the endolysosomal pathway (Hurley and Emr, 2006; Hurley, 2008; Rusten et al., 2011). As part of the ESCRT complex, hepatocyte growth-factor-regulated tyrosine kinase substrate (HGS), regulates the trafficking, degradation, and recycling of a variety of cell surface receptors (Hislop et al., 2004; Hanyaloglu et al., 2005; Yan et al., 2005; Huang et al., 2009; Villaseñor et al., 2016; Dauner et al., 2017; Haugen et al., 2017). The type of interaction between components of the ESCRT pathway and the endosomal pathway influences the fate of internalized cargo and, ultimately, how cells respond to external stimuli. For instance, although HGS can downregulate the abundance of cell surface receptors by sorting them to lysosomes (Bean et al., 2000; Raiborg et al., 2008; Belleudi et al., 2009), it can also act as an endosomal scaffold that supports cell signaling (Huang et al., 2009; Chanut-Delalande et al., 2010; Huang et al., 2010; Miura and Mishina, 2011). However, little is known about how HGS and the endosomal pathway regulate different signaling cascades in the context of the developing nervous system.

Numerous genes that encode proteins believed to regulate endocytic function have been linked to demyelinating forms of Charcot-Marie-Tooth (CMT) disease (Kalaydjieva et al., 2000; Hunter et al., 2003; Street et al., 2003; Bolis et al., 2007; Chow et al., 2007; Lupo et al., 2009; Sidiropoulos et al., 2012; Horn et al., 2012). Mutations in these genes have cell autonomous effects in Schwann cells, resulting in defective formation or maintenance of myelin sheaths (Barisic et al., 2008; Brennan et al., 2015). The endocytic deficits caused by these mutations include defective endocytosis, inhibition of receptor recycling, and impaired lysosomal sorting (Kachhap et al., 2007; Lupo et al., 2009; Lee et al., 2011, 2012; Pietiäinen et al., 2013). CMT-linked proteins have also been shown to interact with components of the ESCRT pathway and play a role in their stability and localization (Lee et al., 2012; Pietiäinen et al., 2013; Li et al., 2015). For example, mutations in lipopolysaccharide-induced tumor necrosis factor (LITAF/SIMPLE) that are linked to demyelinating CMT also reduce endosomal HGS levels (Street et al., 2003; Lee et al., 2012).

We previously showed that a point mutation in *Hgs* (Hgs^{tn}) causes defective myelination (Watson et al., 2015). Although mice that are heterozygous for the Hgs^{tn} allele showed differences in tactile sensitivity and performance in a forced swim test compared with controls (Watson et al., 2015; Meier, 1967), it is not known if the myelination deficit caused by this allele is also inherited in a dominant manner. To examine the cell autonomous effects of loss of HGS on peripheral nerve development, we therefore generated a mouse line that specifically deleted *Hgs* in Schwann cells. Loss of HGS resulted in abnormal myelin sheaths and caused severe motor and sensory deficits similar to those observed in demyelinating CMT (Zoidl et al., 1995; Erdem et al., 1998; Colby et al., 2000; Barisic et al., 2008; Pisciotta and Shy, 2018). HGS-deficient Schwann cells were also hyperproliferative and expressed increased levels of promyelinating genes. In addition to altering the abundance and activation of the myelin-inducing ERBB2/3 receptor tyrosine kinases that traffic through the endosomal pathway in Schwann cells, deletion of *Hgs* also altered the activation of the downstream AKT kinase. These findings suggest a critical role for endosomal sorting of the ERBB2/3 receptors during Schwann cell maturation and for peripheral nerve myelination.

Materials and Methods

Animals. Wild-type C57BL/6J mice were originally obtained from The Jackson Laboratory, and *Hgs*-floxed mice (which we refer to as Hgs^{fl} mice) that contain the $Hgs^{tm1a(EUCOMM)Wtsi}$ allele of *Hgs* were obtained from Helmholtz Zentrum Müenchen German Research Center for Environmental Health. Hgs^{fl} mice contain *loxP* sites in the intronic sequences that flank exon 5 of the *Hgs* gene and were maintained on a C57BL/6J background. These control Hgs^{fl} mice were indistinguishable from wild-type C57BL/6J mice. To delete exon 5 of the *Hgs* gene specifically in Schwann cells, Hgs^{fl} mice were crossed to hemizygous *P0Cre* mice (B6N.FVB-Tg(*Mpz-Cre*)26Mes/J), which were purchased from The Jackson Laboratory (stock #017927). These *P0Cre* transgenic mice express Cre recombinase under the control of the myelin protein zero (P_0, *Mpz*) promoter as early as embryonic day 14 (Feltri et al., 1999). As a result, exon 5 of the *Hgs* gene is specifically deleted in the Schwann cells of the resulting C57BL/6-*Tg(Mpz-cre)26Mes* $Hgs^{tm1fl/fl}$ mice (which we refer to as $P0CreHgs^{fl}$ mice), which were used in all subsequent experiments.

All mouse strains have been maintained in our breeding colony at the University of Alabama at Birmingham, which is fully accredited by the Association for Assessment and Accreditation of Laboratory Animal Care International (A3255-01). All efforts were made to minimize animal suffering, and all research was performed in compliance with the U.S. Animal Welfare Act and other federal statutes and regulations relating to animals. Our studies adhered to the principles stated in the *Guide for the Care and Use of Laboratory Animals* of the National Research Council. In addition, all experiments were conducted with the approval of the University of Alabama at Birmingham Institutional Animal Care and Use Committee (Protocol No. 21800). To ensure that there was no gender bias, equal numbers of both female and male mice were used in this study, and gender difference did not influence any of the reported outcomes.

For genotyping mice, tail DNA was obtained by alkaline lysis extraction, and polymerase chain reactions were performed using MangoTaq polymerase (catalog #BIO-21083, Meridian Biosciences) according to the instructions of the manufacturer. Mice were genotyped for the Hgs^{fl} allele using forward primer 5′-AAGGGGGACACACAAGCAAAA-3′ and reverse primer 5′-CAGCTGAGACTGCTGTGACA-3′, and the presence of the *P0Cre* transgene was identified using forward primer 5′-CCACCACCTCTCCATTGCAC-3′ and reverse primer 5′-ATGTTTA GCTGGCCCAAATG-3′. Thermocycling conditions were one cycle at 94°C for 2 min, 25 cycles at 94°C for 30 s, 58°C for 30 s, and 72°C for 30 s, followed by a single hold at 72°C for 7 min and then held at 4°C until resolution by agarose gel electrophoresis.

Body and muscle mass analysis. Total body and gastrocnemius muscle masses were obtained from 1- and 4-month-old $P0CreHgs^{fl}$ mice and Hgs^{fl} controls. Masses were collected from at least five animals per genotype, with equal numbers of male and female mice used for each genotype, and the values are reported as the average muscle or body mass ± SEM. Unpaired Student's *t* tests were performed to determine statistical significance.

Behavioral analysis. Motor and sensory performance of Hgs^{fl} control mice and $P0CreHgs^{fl}$ mice were evaluated at both 1 and 4 months of age from at least five animals per genotype, with equal numbers of male and female mice used for each genotype. Mice were handled at least 2 d before open field testing. Before each behavioral assay, mice were allowed to habituate to the testing room for 30 min. On the test day, mice were placed in the center of an open field arena (43 × 43 × 30 cm Plexiglas box), locomotion was measured for 5 min by photograph beam detectors, and recorded data were analyzed using ENV-515 software (Med Associates).

Motor coordination and balance were assessed by placing mice on an accelerating rotarod (ENV-575, Med Associates) and recording latency

to fall. The rotarod began rotating at 3.5 revolutions per minute (rpm) and accelerated to 35 rpm over a 5 min period. Each mouse performed three trials a day, with a 15 min intertrial rest period, for 3 consecutive days. The presented latency to fall is the average of the three daily averages for each mouse.

The Chatillon AMETEK Force Gauge was used to assay forelimb grip strength, and the maximum amount of force generated by the forelimbs was recorded. Each mouse trial consisted of 12 repetitions of the assay with the two highest and two lowest data points dropped from final analysis. Unpaired Student's *t* tests were performed to determine statistical significance.

To test tactile sensitivity, mice were assessed using the von Frey filaments test. Animals were habituated to an open gridded floor chamber for 10 min. A series of 12 von Frey fibers ranging from 0.02 to 8 g of force (North Coast Medical) was applied from below the mesh grid in ascending order beginning with the smallest fiber. Fiber application was limited to the central region of the plantar surface to avoid the foot pads, and the hindpaw withdrawal threshold was determined. Unpaired Student's *t* tests were performed to determine statistical significance.

Sciatic nerve morphology. Sciatic nerves were dissected from Hgs^{fl} and $P0CreHgs^{fl}$ mice, fixed in 3% paraformaldehyde/2% glutaraldehyde in 0.2 M sodium cacodylate buffer for 1.5 h, washed in 0.2 M sodium cacodylate, and then postfixed in 1% osmium tetroxide for 1 h in the dark. After thoroughly washing with 0.2 M sodium cacodylate, samples were dehydrated in a graded acetone series of increasing concentration (50, 75, 90, 95, 100% × 4) for 10 min each step and infiltrated with epoxy resin (Electron Microscopy Sciences) by rotating samples overnight in a 1:1 epoxy/acetone solution. The following day, samples were rocked in fresh 100% epoxy for at least 3 × 2 h, embedded, then polymerized in resin overnight at 65°C. Ultrathin cross-sections were collected using a Leica EM-UC6 ultramicrotome and stained for contrast with uranyl acetate and lead citrate. Samples were viewed using an FEI Tecnai T-12 electron microscope with a Hamamatsu digital camera.

Images for morphometric analysis were acquired from adjacent but nonoverlapping fields to measure large-caliber axons (diameter >1 μm), myelin thickness, and axonal density. The g-ratio was calculated by dividing the axon diameter by the axon plus myelin diameter, and the relevant measurements were obtained with ImageJ software (National Institutes of Health). At least 106 axons were quantified across at least two separate fields for each animal. Micrographs taken at 470× magnification were used to measure the number of myelinated fibers, and micrographs taken at 1100× magnification were used to determine g-ratios. The Kolmogorov–Smirnov test was used to determine differences in the frequency of axon diameters.

Protein isolation. Mice were deeply anesthetized with 5% isoflurane to minimize pain and distress before rapid decapitation. Sciatic nerves and brains were dissected and homogenized in modified RIPA buffer containing 50 mM Tris, pH 7.5, 150 mM NaCl, 5 mM $MgCl_2$, 0.5 mM EGTA, 1 mM EDTA, 0.5% SDS, 1% Triton X-100, and 1% sodium deoxycholate. Complete protease inhibitor (Thermo Fisher Scientific), phosphatase inhibitor cocktail III (Thermo Fisher Scientific), iodoacetamide (Sigma-Aldrich), and *N*-ethylmaleimide (Sigma-Aldrich) were added to the homogenization buffer according to the instructions of the manufacturer. Tissues were disrupted using a mechanical homogenizer. Following homogenization, samples were sonicated and centrifuged at 17,000 × *g* for 10 min at 4°C to remove any insoluble material, and supernatants were stored at −20°C. Protein concentrations were determined using the BCA protein assay kit (Thermo Fisher Scientific).

Immunoblotting. Proteins were resolved on either 12 or 4–20% polyacrylamide gels and transferred onto nitrocellulose membranes. A solution of 2% bovine serum albumin (BSA) in tris-buffered saline with 0.1% Tween 20 (TBST) was used to block the membranes. Primary and secondary antibodies (Abs) were diluted in a solution containing 0.5% BSA in TBST. Primary Abs were used at a dilution of 1:1000 and included the following: rabbit anti-HGS (catalog #15087, Cell Signaling Technologies; RRID:AB_2798700), mouse anti-HGS (catalog #sc-271925, Santa Cruz Technologies), mouse anti-MBP (myelin basic protein; catalog #sc-271524, Santa Cruz Technologies), mouse anti-MPZ (myelin protein zero; catalog #sc-18 53, Santa Cruz Technologies), rabbit anti-ERBB2 (catalog #4290, Cell Signaling Technologies), rabbit anti-pERBB2 (catalog #2243, Cell Signaling Technologies), rabbit anti-ERBB3 (catalog #4754, Cell Signaling Technologies; RRID:AB_10691324), rabbit anti-pERBB3 (catalog #4791, Cell Signaling Technologies; RRID:AB_2099709), rabbit anti-AKT (catalog #9279, Cell Signaling Technologies; RRID:AB_331152), rabbit anti-pAKT308 (catalog #9611, Cell Signaling Technologies; RRID:AB_330302), rabbit anti-pAKT473 (catalog #4060, Cell Signaling Technologies), rabbit anti-ERK (catalog #4695, Cell Signaling Technologies), rabbit anti-pERK (catalog #4370, Cell Signaling Technologies), rabbit anti-GSK3β (catalog #9315, Cell Signaling Technologies), rabbit anti-pGSK3β (catalog #9323, Cell Signaling Technologies), rabbit anti-NF2 (catalog #6995, Cell Signaling Technologies), rabbit anti-pNF2 (catalog #9163, Cell Signaling Technologies). Mouse anti-ACTB (Actin-Beta; catalog #ab3280, Abcam; RRID:AB_303668) was used as a loading control. The goat anti-mouse horseradish peroxidase-conjugated secondary Ab (catalog #6420-05, Southern Biotechnology Associates) and goat anti-rabbit horseradish peroxidase-conjugated secondary Ab (catalog #3030-05, Southern Biotechnology Associates) were used at a 1:6000 dilution. SuperSignal West Pico Chemiluminescent Substrate (Thermo Fisher Scientific) was applied to each nitrocellulose membrane and allowed to incubate for 5 min before exposing to film. Blots were cropped to show reactive bands.

RNA-Seq library preparation and sequencing. Total RNA from postnatal day (P)14 sciatic nerves was isolated using RNA-STAT60 (Tel-Test). mRNA sequencing was performed on the Illumina NextSeq500 as described by the manufacturer. Briefly, RNA quality was assessed using the Agilent 2100 Bioanalyzer. RNA with an RNA Integrity Number of $\geq$7.0 was used for sequencing library preparation. RNA passing quality control was converted to a sequencing-ready library using the NEBNext Ultra II Directional RNA library kit as per the instructions of the manufacturer (New England Biolabs). The cDNA libraries were quantitated using qPCR in a Roche LightCycler 480 with the Kapa Biosystems kit for Illumina library quantitation before cluster generation. Cluster generation was performed according to the recommendations of the manufacturer for onboard clustering. We generated between 30 and 35 million paired-end 75 bp sequencing reads per sample for transcript level abundance.

Data assessment and systems biology analysis. STAR software (version 2.7.3a) was used to align the raw RNA-Seq fastq reads to the GRCm38 p6 Release M24 reference genome from Gencode (Dobin et al., 2013). Following alignment, the Dob-count package (version 0.13.5) was used to count the number of reads mapping to each gene (Anders et al., 2015). Normalization and differential expression was then applied to the count files using the DESeq2 package (Love et al., 2014). For generating networks, a dataset containing gene identifiers and corresponding expression values was uploaded into Ingenuity Pathway Analysis. Each identifier was mapped to its corresponding object in the Ingenuity Knowledge Base. A fold change cutoff of $\pm$2 and padj $<$0.05 were set to identify molecules whose expression was significantly differentially regulated. These molecules, called Network Eligible molecules, were overlaid onto a global molecular network developed from information contained in the Ingenuity Knowledge Base. Networks of Network Eligible Molecules were then algorithmically generated based on their connectivity. The Functional Analysis identified the biological functions and/or diseases that were most significant to the entire dataset. Molecules from the dataset that met the fold change cutoff of $\pm$2 and padj $<$0.05 and that were associated with biological functions and/or diseases in the Ingenuity Knowledge Base were considered for the analysis. Right-tailed Fisher's exact test was used to calculate a *p* value determining the probability that each biological function and/or disease assigned to that dataset was because of chance alone.

Quantitative PCR. Total RNA was isolated from the gastrocnemius muscles and sciatic nerves of Hgs^{fl} and $P0CreHgs^{fl}$ mice using RNA-STAT60 and reverse transcribed using the SuperScript VILO cDNA synthesis kit (Thermo Fisher Scientific). Individual gene assays were purchased from Applied Biosystems and included *Achra* (Mm00431629_m1), *Achrb* (Mm00680412_m1), *Achrg* (Mm00437419_m1), *Achre* (Mm00437411_m1), *Nrg1* (Mm01212130_m1), *Cd44* (Mm01277165_m1), *Btc* (Mm00432137_

m1), *Erbb2* (Mm00658541_m1), *Erbb3* (Mm01159999_m1), *Erbb4* (Mm01256796_m1), *Hdac1/2* (Mm02745760_g1), *Sox10* (Mm01300162_m1), *Nfatc4* (Mm00452375_m1), *Sox2* (*Mm03053810_s1*), *Pou3f1* (Mm00456392_m1), *Pou3f2* (Mm00843777_s1), *c-Jun* (*Mm07296811_s1*), *Krox20* (Mm00456650_m1), *Nab1* (Mm01257272_m1), *Srebp* (Mm00550338_m1), *Mpz* (Mm00485141_g1), *Pmp22* (Mm01333393_m1), and *Mbp* (Mm01266402_m1). The TaqMan gene assay for *Actb* (Mm026195800_g1) served as an internal control. The qPCR results are shown as the average of three cDNA amplifications generated from three mice performed in triplicate.

Sciatic nerve immunohistochemistry. Sciatic nerves were rapidly dissected and submerged overnight in 4% paraformaldehyde (Sigma-Aldrich) in PBS and cryoprotected in 30% sucrose (Fisher Scientific) overnight before being embedded in optimal cutting temperature compound (Fisher Scientific) and frozen at −80°C. Cryosections were cut at 10 µm on a Leica 1850 cryostat, mounted on Superfrost charged slides, and stored at −80°C. Nerve sections were blocked with 10% normal goat serum, 1% BSA, and 0.1% Triton X-100. Primary Abs and Alexa Fluor–labeled secondary Abs (catalog #A16071, Thermo Fisher Scientific; RRID:AB_ 2534744 and catalog #A16071, Thermo Fisher Scientific; RRID:AB_2536524) were diluted 1:500 in PBS containing 2% normal goat serum, 0.1% BSA, and 0.1% Triton X-100. Primary mouse anti-HGS (Bean et al., 2000) and rabbit anti-Ki67 (catalog #ab15580, Abcam; RRID:AB_443209) Abs were incubated overnight at 4°C. Sections were washed three times with PBS containing 0.1% Triton X-100 and then incubated with secondary Abs for 1 h at room temperature. Sections were then washed three times with PBS containing 0.1% Triton X-100 and stained with DAPI. Images were acquired using a Zeiss LSM-800 Airyscan confocal microscope (Carl Zeiss).

Teased sciatic nerves were isolated from P14 mice and submerged in Bouin's fixative (RICCA Chemical) for 15 min at 4°C. Nerves were then washed three times in ice-cold PBS and stored overnight at 4°C. The perineurial sheath was then removed, and axons were separated on Superfrost slides using a tuberculin needle. Slides were dried overnight at room temperature and stored at −80°C. Nerves were then permeabilized with methanol for 15 min at −20°C. Sections were blocked with 2.5% normal donkey serum, 2.5% BSA, and 0.5% Triton X-100. Primary mouse anti-HGS (Bean et al., 2000) and rabbit anti-EEA1 (catalog #PA5-17228, Thermo Fisher Scientific; RRID:AB_11004515) Abs were diluted 1:200 in 2.5% normal donkey serum, 2.5% BSA, and 0.5% Triton X-100 and incubated overnight at 4°C. Sections were washed three times with PBS at room temperature and then incubated with secondary antibodies labeled with Alexa Fluor dye (catalog #A16071, Thermo Fisher Scientific; RRID:AB_2534744 and catalog #F-2761, Thermo Fisher Scientific; RRID:AB_2536524) for 1 h at room temperature. Sections were washed three times with PBS and then stained with DAPI. Images were acquired using a Zeiss LSM-800 Airyscan confocal microscope (Carl Zeiss).

Muscle and neuromuscular junction analysis . For whole-mount immunostaining, mice were killed, and the tibialis anterior muscles were rapidly dissected and fixed in 2% paraformaldehyde for 1 h at 4°C. Muscles were teased into fiber bundles and then washed with wash buffer (PBS containing 1% Triton X-100) three times at room temperature for 15 min. Muscle bundles were then blocked with wash buffer containing 2% BSA and 4% normal goat serum for 1 h. To label AChRs, samples were incubated with 1 μg/ml α-bungarotoxin conjugated with tetramethylrhodamine isothiocyanate (Thermo Fisher Scientific) for 1 h. After being washed three times at room temperature for 15 min with wash buffer, muscle fibers were incubated with primary Abs for 2 d at 4°C.

Primary Abs were diluted 1:400 for mouse anti-neurofilament heavy chain and 1:200 for mouse anti-synaptic vesicle protein 2 (SV2; Developmental Studies Hybridoma Bank) in PBS containing 1% BSA, 10% normal goat serum, and 0.1% Triton X-100. After being washed three times for 15 min at room temperature, samples were incubated with secondary Abs conjugated with Alexa Fluor 488 dye (Invitrogen) at a 1:500 dilution for 1 d at 4°C. Samples were then washed three times for 30 min at room temperature, mounted in PBS containing 50% glycerol, and stored at −20°C. Images were captured using a Zeiss LSM-800 Airyscan confocal microscope. The size of all endplates within the area captured were determined by tracing the circumference of the α-bungarotoxin-positive postsynaptic AChR cluster and computing the area using ImageJ software. The extent of overlap between the presynaptic and postsynaptic structures was determined by examining 100 randomly selected muscle and neuromuscular junctions (NMJs) in each muscle (Seburn et al., 2006). Junctions where the nerve completely overlapped the AChRs on the muscle were defined as fully innervated, NMJs with vacant receptor territory were defined as partially innervated, and AChR plaques with no nerve associated were defined as denervated.

Nerve electrophysiology. Bilateral sciatic motor nerve conduction studies (Ubogu et al., 2012; Dong et al., 2016, 2017) were performed on each mouse using a portable Keypoint version 5.11 electrodiagnostic system (Alpine Biomed) with waveforms displayed on a Tecra S3 LCD monitor (Toshiba America). The distal latency, distal and proximal compound motor action potential (CMAP) amplitude and duration, conduction velocity, and total waveform duration were recorded for each mouse. Recordings made from both nerves were averaged for each animal.

Data analysis. Western blots were digitized, and band densities were quantified with UN-SCAN-IT gel digitizing software (Silk Scientific). Pixel totals were recorded and normalized to the level of ACTB. Protein levels were reported as pixel density relative to controls. An unpaired Student's *t* test was performed to determine statistical significance. All data were analyzed using Prism GraphPad software by plotting the average ±SEM. A minimum of four sciatic nerve extracts from each genotype were analyzed for each protein of interest.

Results

Schwann cell-specific deletion of *Hgs*

Our previous studies demonstrated that a methionine to valine substitution in the cargo-binding domain of HGS caused motor and sensory neuropathies in *teetering* mice (Watson et al., 2015). Because HGS function was altered in all cell types in the *teetering* mice, we could not differentiate whether the neurologic defects were because of disruption of HGS in neurons or in Schwann cells. We therefore created a mouse line that specifically deleted *Hgs* in Schwann cells to test whether the loss of HGS in Schwann cells is sufficient to cause a peripheral neuropathy. To inactivate *Hgs* in Schwann cells, we crossed Hgs^{fl} mice, in which exon 5 of *Hgs* is flanked by *loxP* sites, with *P0Cre* transgenic mice that express Cre recombinase from the myelin protein zero promoter (*Mpz*/P_0; Feltri et al., 1999). The *P0Cre* promoter has been extensively used to ablate the expression of genes specifically within Schwann cells (Bolis et al., 2005; Berti et al., 2011; Orita et al., 2013; Beirowski et al., 2014; Grove et al., 2017; Alvarez-Prats et al., 2018). In the resulting $P0CreHgs^{fl}$ mice, Cre-mediated recombination deleted exon 5 of the *Hgs* gene in Schwann cells, enabling us to investigate the role of HGS during peripheral nerve myelination.

To assess Cre-mediated DNA recombination of the Hgs^{fl} allele, reverse transcription PCR with primers that bordered exons 4 and 6 was used to examine RNA from the sciatic nerves of P14 $P0CreHgs^{fl}$ and Hgs^{fl} mice. Whereas a single band that corresponds to the 634 bp DNA fragment expected from exons 4, 5, and 6 of *Hgs* was produced from the Hgs^{fl} sciatic nerve RNA, two distinct DNA fragments were generated from the RNA obtained from the sciatic nerves of the 2-week-old $P0CreHgs^{fl}$ mice (Fig. 1*A*). The larger, less abundant band was the same size as that found in the Hgs^{fl} controls, and the smaller, more prominent band was consistent with the expected 510 bp fragment that contains exons 4 and 6 but lacks exon 5 of *Hgs* (Fig. 1*A*). DNA sequencing of the two fragments generated from the $P0CreHgs^{fl}$ mice verified that the larger band represented the typical splicing pattern of *Hgs*, whereas the faster migrating band contained a

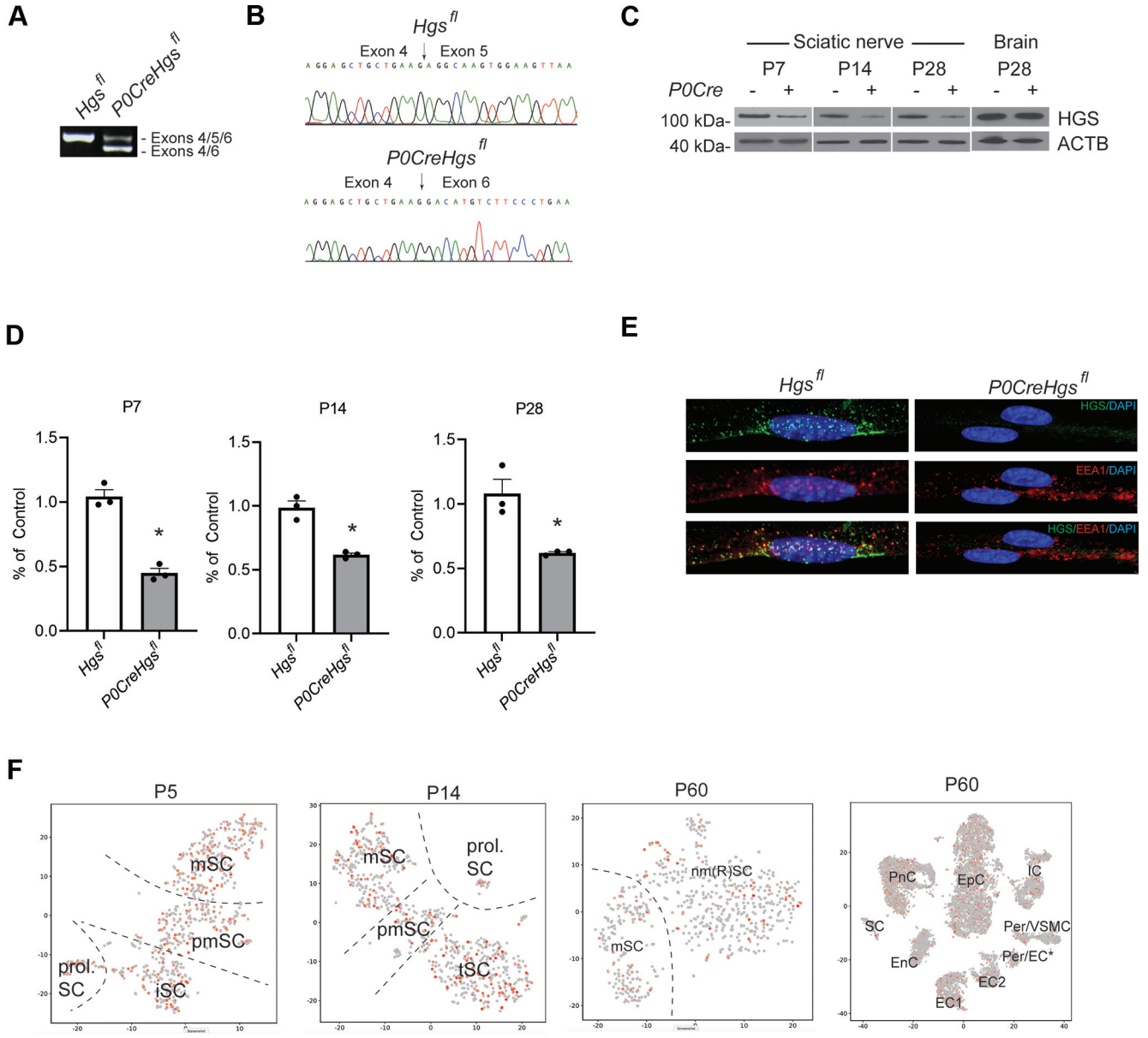

Figure 1. Schwann-cell-specific deletion of *Hgs*. ***A***, Agarose gel electrophoresis of the RT-PCR products generated from the sciatic nerves of P14 *Hgs*^{fl} and *P0CreHgs*^{fl} mice using primers that flank exons 4 and 6 (***A***). The wild-type *Hgs*^{fl} allele contains exons 4, 5, and 6 of *Hgs*, whereas the conditional allele generated from Cre-mediated deletion of exon 5 only contains exons 4 and 6 as confirmed by (***B***) DNA sequence analysis of the RT-PCR products showing the splicing pattern of the *Hgs* mRNA. The arrows indicate the splice site junctions between either exons 4 and 5 in the wild-type allele or exons 4 and 6 in the conditional allele. ***C***, ***D***, Representative immunoblot (***C***) and quantitation (***D***) showing reduced HGS levels in sciatic nerve extracts from *P0CreHgs*^{fl} (*P0Cre*+) mice at P7 ($p = 4.61 \times 10^{-6}$), P14 ($p = 1.19 \times 10^{-6}$), and P28 ($p = 8.58 \times 10^{-6}$) but not in total brain extracts from P28 *P0CreHgs*^{fl} mice ($p = 0.26$) relative to *Hgs*^{fl} controls (*P0Cre*-). ACTB was used as a loading control. Data are shown as mean ± SEM; $n = 3$. Student's *t* test was used to determine whether there was a significant difference in the means of the datasets. ***E***, Immunofluorescence showing localization of HGS (green), EEA1 (red), and DNA (DAPI, blue) in teased sciatic nerve sections from P14 *P0CreHgs*^{fl} and *Hgs*^{fl} control mice. ***F***, Transcriptomics of sciatic nerves demonstrating HGS expression in proliferating Schwann cells (prol. SC), immature Schwann cells (iSC), promyelinating Schwann cells (pmSC), mature Schwann cells (mSC), transition Schwann cells (tSC), nonmyelinating (Remak) Schwann cells (nm(R)SC), perineurial cells (PnC), endoneurial cells (EnC), epineurial cells (EpC), endothelial cells 1 (EC1), endothelial cells 2 (EC2"), immune cells (IC), pericytes and vascular smooth muscle cells (Per/VSMC), and pericytes/endothelial cells (Per/EC*) over various stages of postnatal development (Gerber et al., 2021). Representative immunoblot using an antibody recognizing the aminoterminus of HGS is shown in Extended Data Figure 1-1. * indicates $p < 0.05$.

deletion of exon 5 (Fig. 1*B*). Whereas the *Hgs*^{fl} allele is predicted to generate a 776 amino acid protein, the deletion of exon 5 in the *P0CreHgs*^{fl} mice is expected to result in a frame-shift mutation that truncates HGS after 140 amino acids. Although we have not detected this truncated form in *P0CreHgs*^{fl} sciatic nerves using an antibody that recognizes the N terminus of HGS (Extended Data Fig. 1-1), this fragment of HGS lacks the FYVE domain that is essential for HGS to bind to endosomes.

Immunoblot analysis confirmed reduced HGS expression in sciatic nerve extracts from 1- to 4-week-old *P0CreHgs*^{fl} mice relative to controls (Fig. 1*C*,*D*). This decrease in HGS expression was not observed in brain extracts from 4-week-old *P0CreHgs*^{fl} mice (Fig. 1*C*,*D*), which is consistent with the specificity of the *P0Cre* promoter for Schwann cells. Immunostaining for HGS also showed a substantial reduction in HGS in teased sciatic nerves from 2-week-old *P0CreHgs*^{fl} mice compared with controls. In control mice, HGS was detected in an expected punctate-like

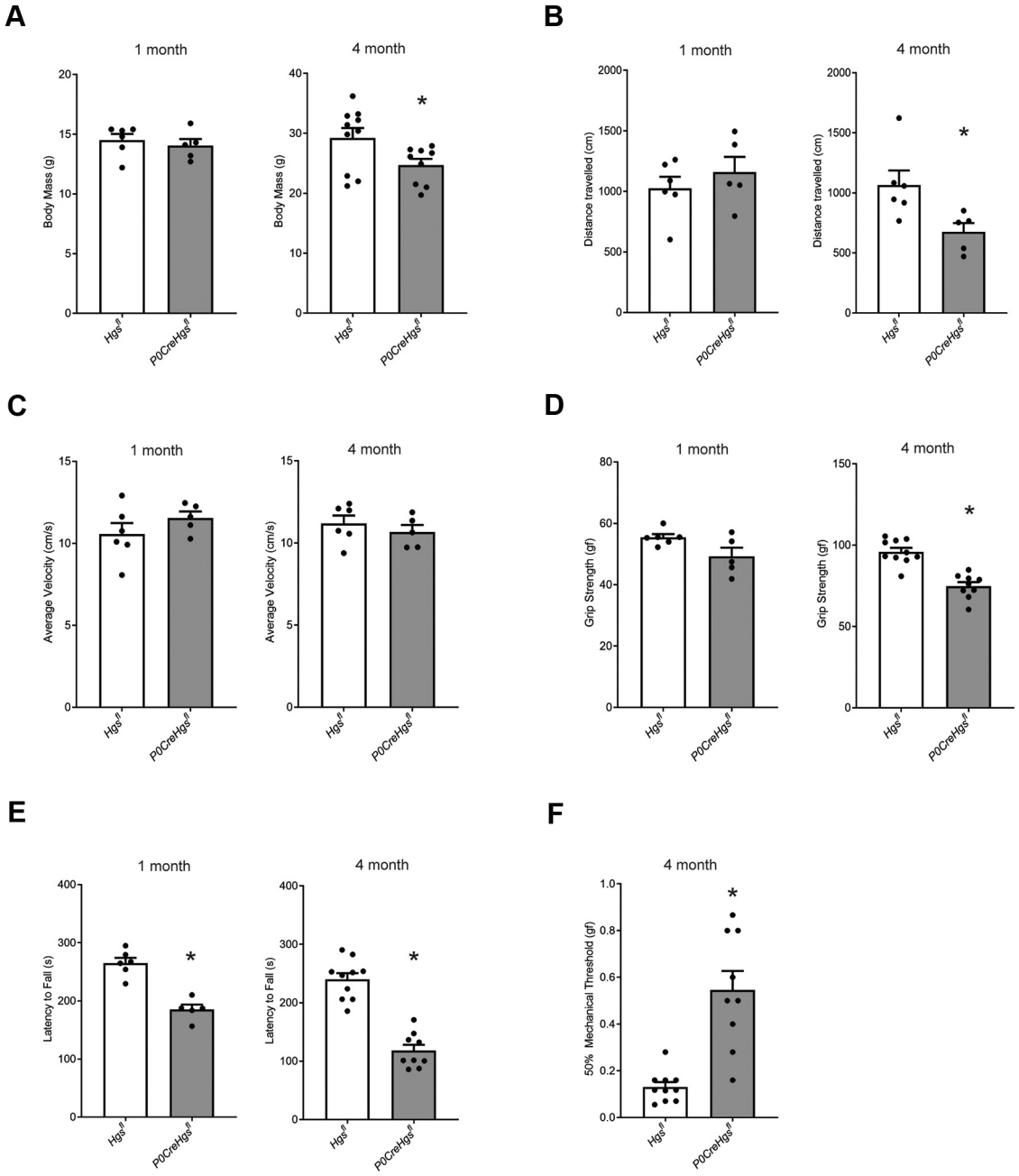

Figure 2. Motor and sensory function in *Hgs*^{fl} and *P0CreHgs*^{fl} mice. ***A***, Total body mass (1 month $p = 0.62$, 4 month $p = 0.035$). ***B***, Distance traveled in open field (1 month $p = 0.53$, 4 month $p = 0.0087$). ***C***, Average velocity in open field (1 month $p = 0.32$, 4 month $p = 0.42$). ***D***, Forelimb grip strength. grams force (gf; 1 month $p = 0.16$, 4 month $p = 8.66 \times 10^{-5}$. ***E***, Latency to fall during rotarod analysis (1 month $p = 0.0043$, 4 month $p = 1.0 \times 10^{-5}$) of *Hgs*^{fl} and *P0CreHgs*^{fl} mice. ***F***, Mechanical allodynia determined by von Frey assay of *Hgs*^{fl} and *P0CreHgs*^{fl} mice ($p = 1.4 \times 10^{-4}$). Data are shown as mean ± SEM; $n > 5$ mice per genotype. Mann–Whitney test was used to determine whether there was a significant difference in the means of the datasets. Representative open field traces for 4-month-old *Hgs*^{fl} and *P0CreHgs*^{fl} mice are shown in Extended Data Figure 2-1. * indicates $p < 0.05$.

pattern in the cytosol that partially overlapped the staining of the early endosomal antigen EEA1 (Fig. 1*E*).

A transcriptome database was recently generated to determine the developmental and cellular profile of genes expressed in sciatic nerves (Gerber et al., 2021). Examination of this database revealed that HGS is expressed in proliferating, immature, promyelinating, mature, and nonmyelinating Schwann cells (Fig. 1*F*). HGS expression was also detected in perineurial cells, endoneurial cells, epineurial cells, immune cells, pericytes, vascular smooth muscle cells, and pericytes/endothelial cells (Fig. 1*F*). Therefore, the low levels of HGS that we detected in the sciatic nerves of the *P0CreHgs*^{fl} mice by both immunoblotting and immunofluorescence likely represent HGS expression in these other cell types. This residual level of gene expression is similar to what has been reported when *P0Cre* has been used to delete other floxed alleles (Beirowski et al., 2014; Gomez-Sanchez et al., 2015; Logan et al., 2017).

Motor and sensory defects in *P0CreHgs*^{fl} mice

P0CreHgs^{fl} mice were born at a Mendelian frequency and were indistinguishable from control *Hgs*^{fl} mice at birth. Although no difference in body mass was detected at 1 month of age, the *P0CreHgs*^{fl} mice were significantly smaller than controls by 4 months of age (Fig. 2*A*). In an open field assay to examine

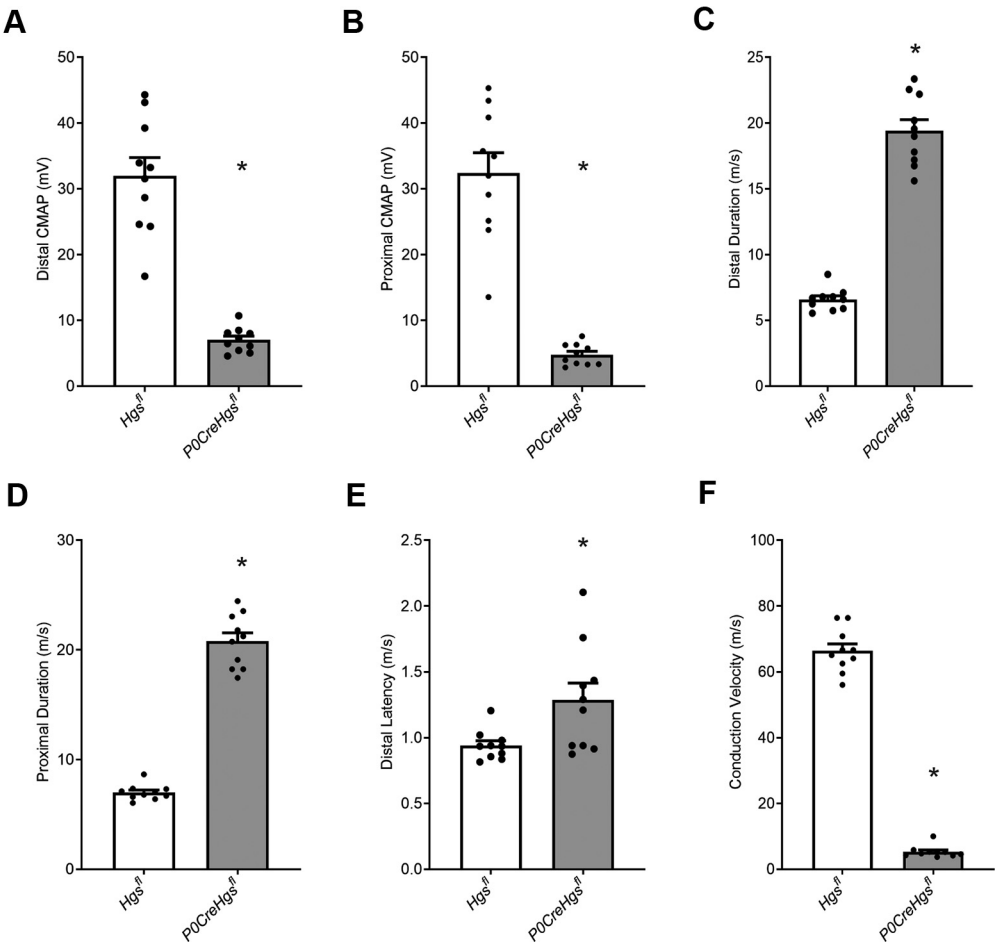

Figure 3. Sciatic nerve electrophysiology in 4-month-old *Hgs*^{fl} and *P0CreHgs*^{fl} mice. ***A***, Amplitude of distal CMAP ($p = 1.08 \times 10^{-5}$). ***B***, Amplitude of proximal CMAP ($p = 1.1 \times 10^{-5}$). ***C***, Distal total waveform duration ($p = 2.02 \times 10^{-11}$). ***D***, Proximal total waveform duration ($p = 1.08 \times 10^{-5}$). ***E***, Distal latency ($p = 0.021$). ***F***, Conduction velocity ($p = 1.1 \times 10^{-5}$) measured from both the right and left sciatic nerves and averaged for each *Hgs*^{fl} and *P0CreHgs*^{fl} mouse. Data are shown as mean ± SEM; $n = 10$ mice per genotype. Mann–Whitney test was used to determine whether there was a significant difference in the means of the datasets. * indicates $p < 0.05$.

overall motor function, 4-month-old *P0CreHgs*^{fl} mice traveled significantly less than controls (Fig. 2*B*; Extended Data Fig. 2-1), but no difference was observed in the average velocity of the *P0CreHgs*^{fl} mice compared with controls (Fig. 2*C*). In addition, the grip strength of the *P0CreHgs*^{fl} mice was significantly reduced at 4 months of age (Fig. 2*D*), and the mice demonstrated a decreased ability to stay on a Rotarod at both 1 and 4 months of age compared with controls (Fig. 2*E*). By 4 months of age, the *P0CreHgs*^{fl} mice also displayed decreased tactile sensitivity when examined using the von Frey assay (Fig. 2*F*). These results indicate that loss of HGS in Schwann cells results in both motor and sensory deficits in the *P0CreHgs*^{fl} mice.

Motor nerve electrophysiology

To determine whether Schwan-cell-specific loss of HGS altered the electrophysiological properties of the peripheral nerves, we measured the amplitudes and durations of the CMAPs of the calf muscles, the distal latency, and the deduced velocities following distal and proximal sciatic nerve stimulation (Fig. 3). Both distal and proximal CMAP amplitudes, which indirectly measure the number of functional myelinated motor axons, were markedly reduced in 4-month-old *P0CreHgs*^{fl} mice compared with controls (Fig. 3*A*,*B*). In addition, the distal and proximal CMAP durations were also significantly increased in the *P0CreHgs*^{fl} mice (Fig. 3*C*,*D*), indicating conduction slowing and/or conduction block of myelinated motor axons. Consistent with these findings, the distal CMAP latency was significantly prolonged (Fig. 3*E*), and the conduction velocity was significantly reduced (Fig. 3*F*) in the *P0CreHgs*^{fl} mice compared with controls, both of which measure the conduction of the fastest conducting motor axons. Together, these abnormal electrophysiological properties indicate that Schwann cell loss of HGS causes a demyelinating peripheral neuropathy.

Delayed myelination in HGS-deficient Schwann cells

We used transmission electron microscopy to examine transverse sections of sciatic nerves from *P0CreHgs*^{fl} and *Hgs*^{fl} mice at P7, P14, P28, and P120 (Fig. 4*A*–*C*). In *Hgs*^{fl} control mice, more than 75% of the large diameter axons (>1 μm) were myelinated at P7, and the proportion of myelinated axons progressively increased so that almost all of the large caliber axons were myelinated by P28 (Fig. 4*A*,*B*), which is consistent with what has been reported for wild-type mice (Hahn et al., 1987). In contrast, the number of myelinated axons in the sciatic nerves of *P0CreHgs*^{fl} mice was significantly reduced at all ages examined (Fig. 4*A*,*B*). Instead of the typical myelinated axons, many promyelinated axons were observed in the sciatic nerves from the P7, P14, and P28 *P0CreHgs*^{fl} mice; these are axons that are ensheathed in a 1:1 ratio by Schwann cells but are not myelinated

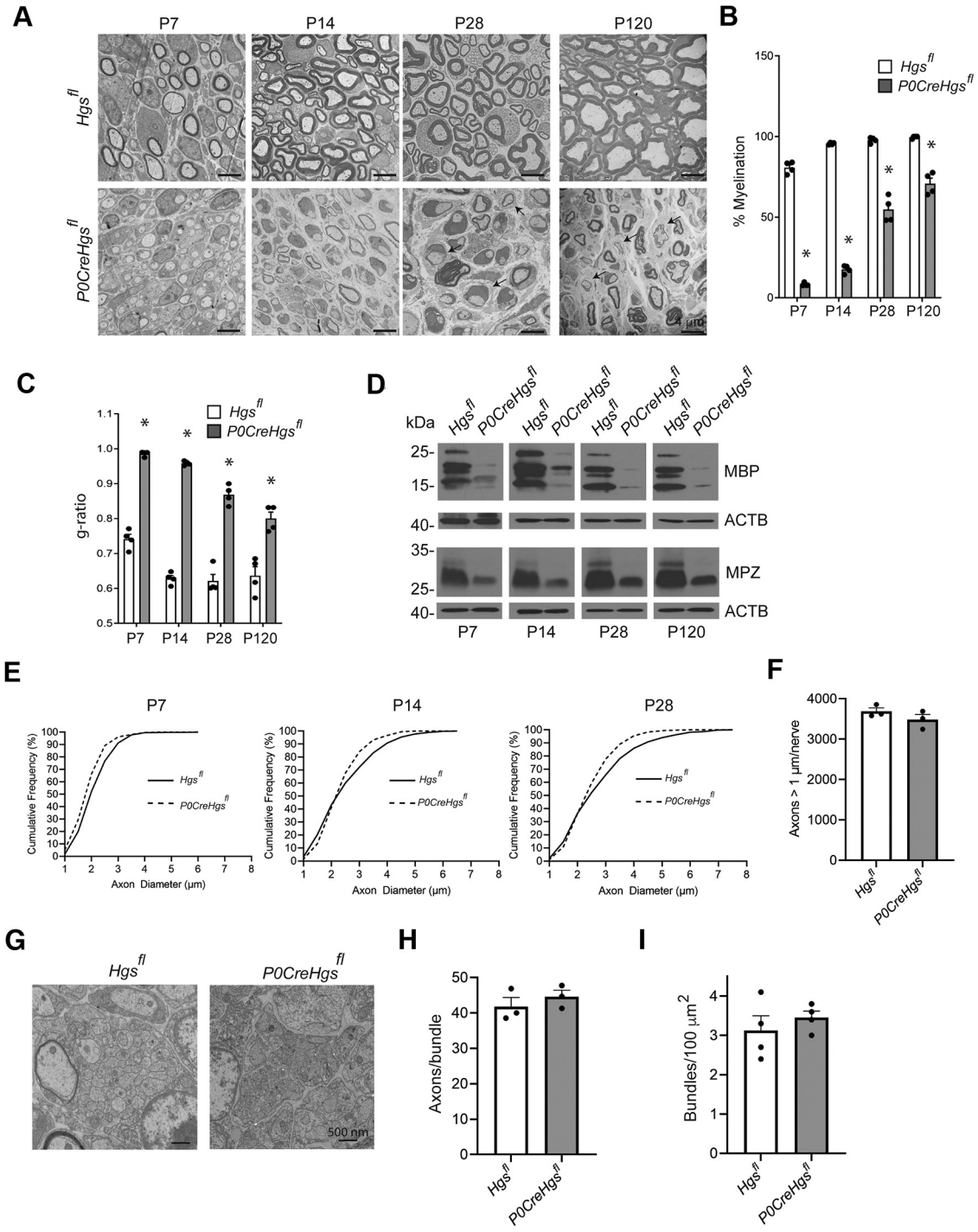

Figure 4. Hypomyelination of sciatic nerves in *P0CreHgs*^{fl} mice. ***A***, Representative electron micrographs of sciatic nerves from P7, P14, P28, and P120 *Hgs*^{fl} and *P0CreHgs*^{fl} mice. Arrows indicate basal lamina onion bulbs. ***B***, Quantitation of the percentage of myelinated axons (P7. $p = 2.11 \times 10^{-5}$; P14, $p = 1.48 \times 10^{-4}$; P28, $p = 3.92 \times 10^{-5}$; P120, $p = 1.48 \times 10^{-4}$). ***C***, The g-ratio (P7, $p = 3.0 \times 10^{-6}$; P14, $p = 3.23 \times 10^{-8}$; P28, $p = 4.4 \times 10^{-5}$; P120, $p = 0.0021$) in sciatic nerves from *Hgs*^{fl} and *P0CreHgs*^{fl} mice. Data are shown as mean ± SEM, $n = 4$. Student's *t* test was used to determine whether there was a significant difference in the means of the datasets. ***D***, Representative immunoblots showing the levels of MBP and MPZ from sciatic nerve extracts of P7, P14, P28, and P120 *Hgs*^{fl} and *P0CreHgs*^{fl} mice. ACTB was used as a loading control. ***E***, Cumulative frequency plots showing the distribution of axon size in *Hgs*^{fl} and *P0CreHgs*^{fl} mice at P7 ($p = 4.61 \times 10^{-6}$), P14 ($p = 1.19 \times 10^{-6}$), and P28 ($p = 8.85 \times 10^{-5}$). The Kolmogorov–Smirnov test was used to determine significance; $n = 4$. ***F***, Quantitation of axons >1 μm in sciatic nerves from 4-month-old *Hgs*^{fl} and *P0CreHgs*^{fl} mice ($p = 0.22$). Data are shown as mean ± SEM; $n = 3$. Student's *t* test was used to determine whether there was a significant difference in the means of the datasets. ***G–I***, Representative electron micrograph of axon bundles and quantitation of (***H***) axons per bundle ($p = 0.9287$, $n = 3$) and (***I***) axon bundles per 100 µm^2 ($p = 0.93$, $n = 4$) from sciatic nerves of P3 *Hgs*^{fl} and *P0CreHgs*^{fl} mice. Data are shown as mean ± SEM. Student's *t* test was used to determine whether there was a significant difference in the means of the datasets. * indicates $p < 0.05$.

(Arroyo et al., 1998). Although promyelinated axons could also be observed in *P0CreHgs*^{fl} mice at P120, because of the presence of basal lamina onion bulbs around some of these axons (Fig. 4*A*) they may also be in the process of being re-ensheathed following segmental demyelination. The myelin sheaths from *P0CreHgs*^{fl} sciatic nerves were also significantly thinner than controls at all ages examined (Fig. 4*C*). The reduced number of myelinated axons and the thinner myelin sheaths in *P0CreHgs*^{fl}

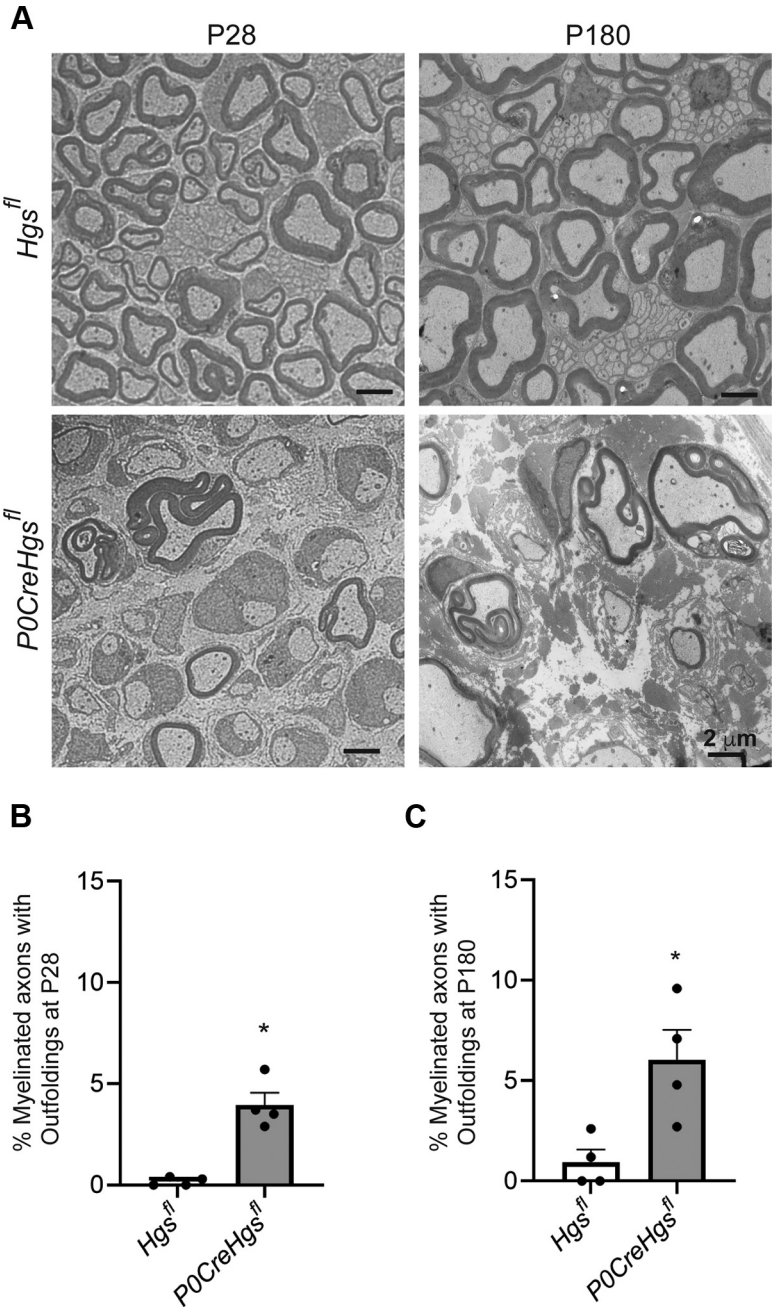

Figure 5. Deletion of HGS in Schwann cells leads to aberrant myelination. ***A–C***, Representative electron micrographs of sciatic nerve sections from P28 and P180 *Hgs*^{fl} and *P0CreHgs*^{fl} mice. ***B***, ***C***, Quantitation of myelin outfoldings in P28 ($p = 0.0002$, ***B***) and P180 ($p = 0.0023$, ***C***) mice. Data are plotted as the percentage of fibers that were found to be defective and are shown as mean ± SEM; $n = 4$. Student's *t* test was used to determine whether there was a significant difference in the means of the datasets. * indicates $p < 0.05$.

nerves correlated with reduced levels of MBP and MPZ in the sciatic nerves of *P0CreHgs*^{fl} mice (Fig. 4*D*).

Because a change in axon diameter has been reported in a number of peripheral neuropathies, we compared the frequency distribution of axonal diameters found in the sciatic nerves of *P0CreHgs*^{fl} mice with controls. We found a significant reduction in axonal diameter at P7, P14, and P28 (Fig. 4*E*), which could also contribute to the hypomyelination observed in the *P0CreHgs*^{fl} mice. To determine whether defective myelination in the *P0CreHgs*^{fl} mice also results in axonal loss, we measured the numbers of large-caliber axons in sciatic nerve sections from control and *P0CreHgs*^{fl} mice at 4 months of age. Despite a significant reduction in myelination (Fig. 4*B*), the number of axons >1 μm in diameter was not significantly different in the *P0CreHgs*^{fl} sciatic nerves compared with controls (Fig. 4*F*). There was also no significant difference in radial sorting of large-diameter axons or the number of unmyelinated axon bundles in the sciatic nerves of P3 *P0CreHgs*^{fl} mice compared with controls (Fig. 4*G–I*).

In addition to causing delayed and reduced myelination, loss of HGS in Schwann cells resulted in aberrantly folded myelin sheaths. These were evident in the sciatic nerves of both P28 and 6-month-old *P0CreHgs*^{fl} mice (Fig. 5*A–C*). Conspicuously folded myelin sheaths have been reported in humans and animal models of other inherited demyelinating neuropathies (Azzedine et al., 2003; Bolino et al., 2004; Bolis et al., 2005; Robinson et al., 2008; Pereira et al., 2012) and are thought to be because of Schwann cell autonomous deficits. Thus, HGS is required for both the proper induction of myelination and the formation of structurally normal myelin sheaths.

Loss of HGS in Schwann cells alters NMJ and muscle development

Several reports have indicated developmental impairment and reduced synaptic transmission at the NMJ in mouse models of CMT (Yin et al., 2004; Ang et al., 2010; Sleigh et al., 2014; Spaulding et al., 2016; Cipriani et al., 2018; Nandini et al., 2019). To investigate whether loss of HGS in Schwann cells also disrupts the NMJ, we first examined the gastrocnemius muscles and found a significant decrease in muscle mass in 4-month-old *P0CreHgs*^{fl} mice compared with controls (Fig. 6*A*). As impaired innervation can result in reduced muscle development and upregulated expression of AChRs (Evans et al., 1987; Goldman et al., 1988; Witzemann, 1989; Ang et al., 2010), we next measured the *AChR* α, β, ε, and γ subunit mRNA levels in the gastrocnemius muscles of 4-month-old *Hgs*^{fl} and *P0CreHgs*^{fl} mice. Although no differences were observed in *AChR* α or ε mRNA levels, there was a significant increase in the levels of both *AChR* β and γ subunit mRNAs in *P0CreHgs*^{fl} mice relative to controls (Fig. 6*B*). As skeletal muscle denervation in animal models results in muscle atrophy and a significant increase in the expression of the *AChR* γ subunit (Witzemann, 1989; Eiber et al., 2019; Cetin et al., 2020), our data suggest that Schwann cell loss of HGS has an impact on synaptic transmission at the NMJ (Goldman et al., 1988; Adams et al., 1995; Kong et al., 2009; Vaden et al., 2015; Watson et al., 2015).

To examine motor endplate structure in the *Hgs*^{fl} and *P0CreHgs*^{fl} mice, we identified motor axons by immunostaining the tibialis anterior muscles for neurofilament (NF) and SV2 and labeled the AChRs with FITC-conjugated α-bungarotoxin (Fig. 6*C*). At 4 months of age, there was a reduction in fully innervated NMJs and a corresponding increase in partially innervated NMJs

in *P0CreHgs*^{fl} mice compared with controls (Fig. 6*C*,*D*). These results suggest that the impaired *AChR* expression and reduced muscle mass in the *P0CreHgs*^{fl} mice are because of changes in NMJ integrity.

Transcriptome analysis of HGS-deficient sciatic nerves

To investigate the cause of arrested sciatic nerve myelination in the *P0CreHgs*^{fl} mice, we performed transcriptome analysis on sciatic nerve RNA from P14 *P0CreHgs*^{fl} and *Hgs*^{fl} control mice. Principal component analysis demonstrated that the results from both the control and the *P0CreHgs*^{fl} sciatic nerves clustered into two distinct groups for each genotype (Fig. 7*A*). Bioinformatics analysis revealed that the expression of 2469 genes was altered at least twofold in the *P0CreHgs*^{fl} sciatic nerves compared with controls (Fig. 7*B*; Extended Data Fig. 7-1), and the top 50 upregulated and top 50 downregulated genes are shown in Figure 7, *C* and *D*. Gene Ontology and pathway analysis revealed an enrichment in genes that regulate cell proliferation, gliogenesis, and myelination in the sciatic nerves of the *P0CreHgs*^{fl} mice (Fig. 7*E*; Extended Data Figs. 7-2, 7-3, 7-4).

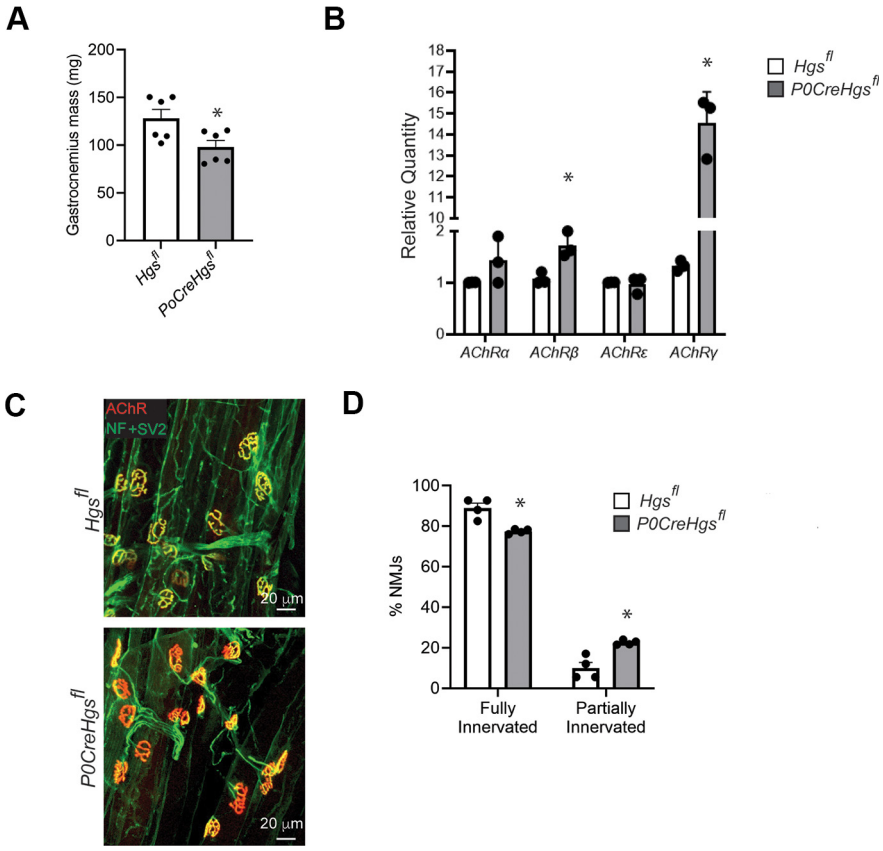

Figure 6. Effects of HGS deletion in Schwann cells on gastrocnemius mass, motor endplate structure, and *AChR* expression. ***A***, Gastrocnemius muscle mass from 4-month-old *Hgs*^{fl} and *P0CreHgs*^{fl} mice ($p = 0.0020$). Data are plotted as mean ± SEM; $n = 6$ mice per genotype. Student's *t* test was used to determine whether there was a significant difference in the means of the datasets. ***B***, qPCR analysis of *AChR-α* ($p = 0.068$), *AChR-β* ($p = 3.0 \times 10^{-5}$), *AChR-ε* ($p = 0.57$), and *AChR-γ* ($p = 5.0 \times 10^{-5}$) mRNAs from the gastrocnemius muscles of 4-month-old *Hgs*^{fl} and *P0CreHgs*^{fl} mice. Data are plotted relative to the amount detected in *Hgs*^{fl} controls and are shown as mean ± SEM; $n = 3$. Student's *t* test was used to determine whether there was a significant difference in the means of the datasets. ***C***, Tibialis anterior muscles from 4-month-old *Hgs*^{fl} and *P0CreHgs*^{fl} mice stained with Abs for NF and SV2 to detect motor neuron terminals (green) and with TRITC-labeled α-bungarotoxin to detect AChRs (red). ***D***, Quantification of NMJs revealed that 89.97% of the NMJs were fully innervated, and 10.03% of the NMJs were partially innervated in the *Hgs*^{fl} mice, whereas 77.45% of the NMJs were fully innervated ($p = 0.0036$), and 22.55% were partially innervated ($p = 0.0046$) in the *P0CreHgs*^{fl} mice at 4 months of age. Data are plotted as mean ± SEM; $n = 4$ mice per genotype. Student's *t* test was used to determine whether there was a significant difference in the means of the datasets. * indicates $p < 0.05$.

Increased cell proliferation in HGS-deficient sciatic nerves

Transcriptome analysis of sciatic nerves from *P0CreHgs*^{fl} mice demonstrated a striking enrichment of genes involved in cell proliferation and cell cycle control. To investigate whether the arrested myelination observed in the *P0CreHgs*^{fl} mice was because of changes in cell proliferation and/or Schwann cell differentiation, we first compared Ki67 staining in control and *P0CreHgs*^{fl} sciatic nerves at P7 and P14. Consistent with a previous report (Brown and Asbury, 1981), we observed the expected reduction in proliferating cells in sciatic nerves from control mice at P14 compared with P7. Although the percentage of Ki67-positive cells was not statistically different between the *P0CreHgs*^{fl} mice and controls at P7 (Fig. 8*A*,*B*), there was a significant increase in the number of proliferating cells in the sciatic nerves of the *P0CreHgs*^{fl} mice compared with controls at P14 (Fig. 8*A*,*C*). These cells likely represent either proliferating Schwann cells or infiltrating immune cells. A similar increase in the number of Ki67-positive cells has previously been found in other animal models of demyelinating neuropathies (Perkins et al., 1981; Sancho et al., 2001) and is consistent with delayed Schwann cell maturation.

Schwann cell differentiation is accompanied by a well-described and distinct pattern of gene expression that defines immature Schwann cells, promyelinating Schwann cells, and myelinating Schwann cells (Jessen and Mirsky, 2005; Salzer, 2015). To confirm our RNA transcriptome analysis that suggests a block in Schwann cell maturation in the *P0CreHgs*^{fl} mice, we examined the expression of several markers of immature, promyelinating and myelinating Schwann cells from RNA isolated from the sciatic nerves of P14 *P0CreHgs*^{fl} and *Hgs*^{fl} mice using qPCR. Although we did not observe any differences in the expression of the immature Schwann cell markers *Hdac1*, *Sox10*, or *Nfatc4* (Fig. 8*D*), there was an increase in the levels of several promyelinating mRNAs, including *Sox2*, *Pou3f1*, *Pou3f2*, and *c-Jun* in the sciatic nerves of the *P0CreHgs*^{fl} mice as compared with controls (Fig. 8*E*). In addition, the mRNA levels for *Egr2*, *Nab1*, *Srebp1*, *Mpz*, *Pmp22*, and *Mbp*, which are markers of myelinating Schwann cells, were reduced in the sciatic nerves of P14 *P0CreHgs*^{fl} mice as compared with controls (Fig. 8*F*). Consistent with our findings on the level of HGS at P14, the level of *Hgs* mRNA was reduced by 70% in the *P0CreHgs*^{fl} sciatic nerves (Fig. 8*F*). Thus, the altered gene expression in HGS-deficient Schwann cells corresponds with the increase in promyelinating Schwann cells observed in the sciatic nerves of the P14 *P0CreHgs*^{fl} mice (Fig. 4*A*).

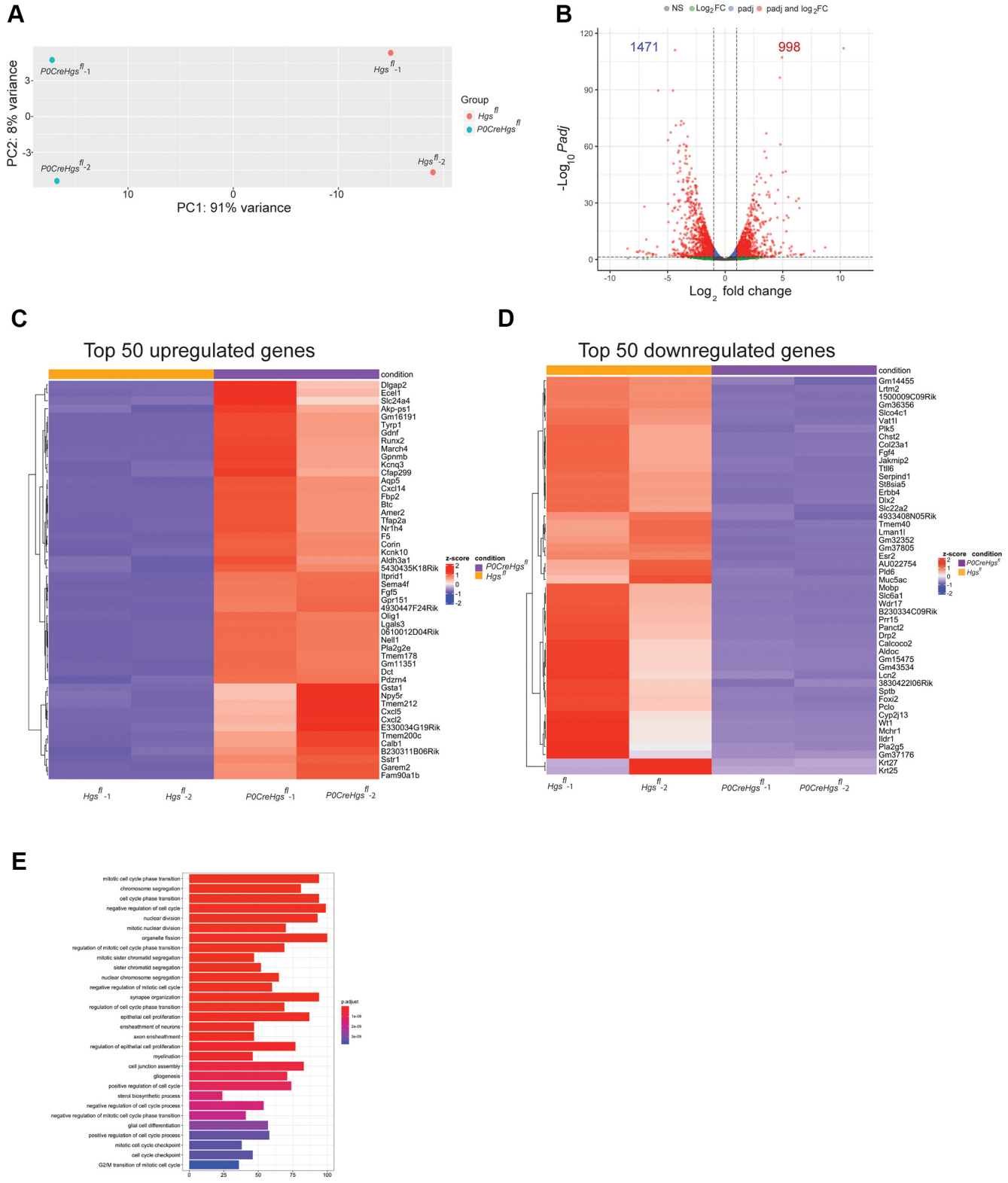

Figure 7. Transcriptome analysis of *Hgs*^{fl} and *P0CreHgs*^{fl} sciatic nerves. ***A***, Principal component analysis results show that gene expression in P14 *Hgs*^{fl} and *P0CreHgs*^{fl} sciatic nerves segregate into two separate groups for each genotype. ***B***, Volcano plot of transcriptome data displaying the pattern of genes altered at least twofold in sciatic nerves of P14 *P0CreHgs*^{fl} mice compared with *Hgs*^{fl} controls ($p < 0.05$). ***C***, ***D***, Heat map of the top 50 significantly upregulated (***C***) and downregulated (***D***) genes in the sciatic nerves of P14 *P0CreHgs*^{fl} mice compared with *Hgs*^{fl} controls. ***E***, Gene Ontology showing the biological processes altered in the *P0CreHgs*^{fl} sciatic nerves compared with controls; $n = 2$ mice per genotype. DESeq2 annotated results with normalized counts for P14 *Hgs*^{fl} and *P0CreHgs*^{fl} transcriptome analysis are shown in Extended Data Figure 7-1. Gene Ontology analysis describing biological pathways, cellular components, and molecular functions altered in the *P0CreHgs*^{fl} sciatic nerves are shown in Extended Data Figures 7-2, 7-3, and 7-4, respectively.

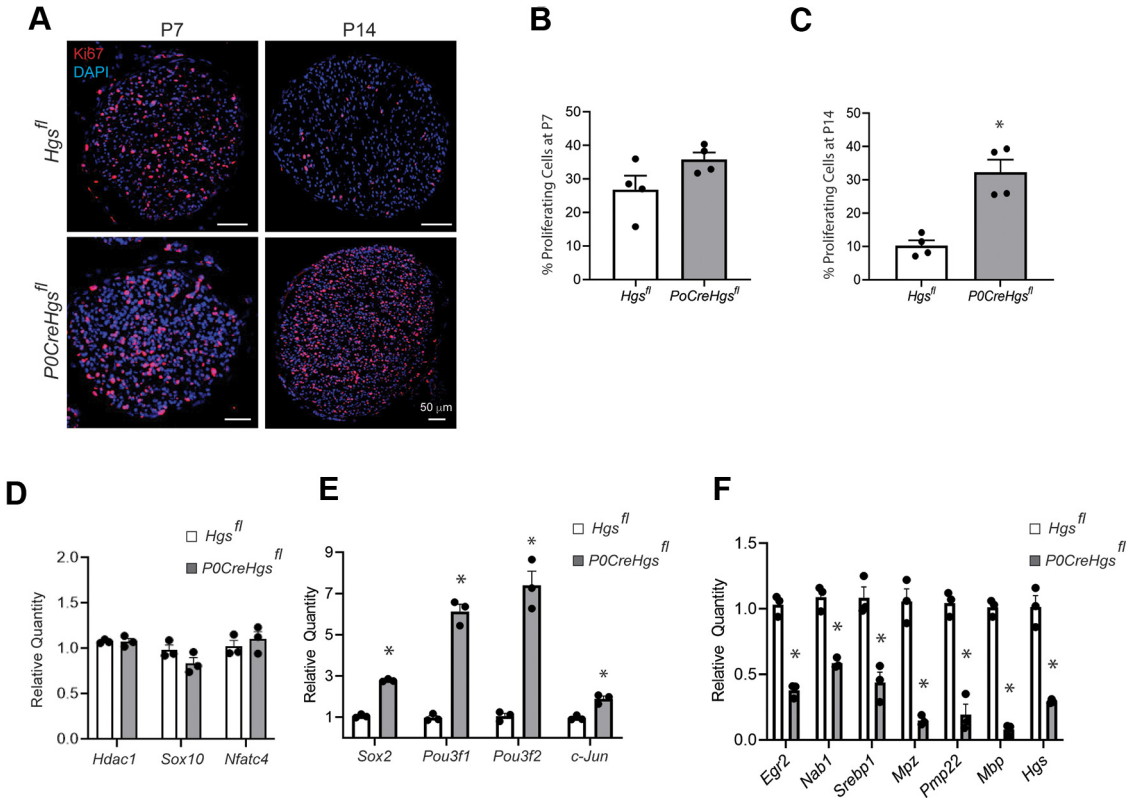

Figure 8. Maturational deficits in HGS-deficient Schwann cells. ***A***, Sciatic nerve sections from (P)7 and P14 *Hgs*^{fl} and *P0CreHgs*^{fl} mice were stained for the proliferating antigen marker Ki67 (red) and with DAPI to detect DNA (blue). ***B***, ***C***, Quantitation of the number of proliferating (Ki67-positive) nuclei from (***B***) P7 ($p = 0.12$) and (***C***) P14 ($p = 4.51 \times 10^{-8}$) *Hgs*^{fl} and *P0CreHgs*^{fl} mice. Data are shown as mean ± SEM; $n = 4$ mice per genotype. Student's *t* test was used to determine whether there was a significant difference in the means of the datasets. ***D–F***, Quantitation of mRNA levels in the sciatic nerves of P14 *P0CreHgs*^{fl} mice for genes that serve as markers of (***D***) immature (*Hdac1*, $p = 0.77$; *Sox10*, $p = 0.15$; *Nfatc4*, $p = 0.50$), (***E***) promyelinating (*Sox2*, $p = 1.0 \times 10^{-4}$; *Pou3f1*, $p = 1.0 \times 10^{-4}$; *Pou3f2*, $p = 8.0 \times 10^{-4}$; *c-Jun*, $p = 0.0032$), and (***F***) myelinating (*Egr2*, $p = 3.0 \times 10^{-4}$; *Nab1*, $p = 0.0011$; *Srebp1*, $p = 0.0050$; *Mpz*, $p = 7.0 \times 10^{-4}$; *Pmp22*, $p = 9.0 \times 10^{-4}$; *Mbp* $p = 4.0 \times 10^{-4}$) Schwann cells relative to levels found in *Hgs*^{fl} controls. The level of *Hgs* mRNA was reduced 70% in *P0CreHgs*^{fl} mice relative to controls ($p = 0.0011$). Data are shown as mean ± SEM; $n = 3$ mice per genotype. Student's *t* test was used to determine whether there was a significant difference in the means of the datasets. * indicates $p < 0.05$.

Alterations in the ERBB2/3 pathway in HGS-deficient Schwann cells

Our transcriptome analysis showed that the NRG1/ERBB signaling pathway was significantly upregulated in the sciatic nerves of the *P0CreHgs*^{fl} mice (Extended Data Figs. 7-1, 7-2). Further examination of the mRNA levels of components in this pathway validated the RNA-Seq results and demonstrated that the levels of *Erbb3, Btc, Nrg1,* and *Cd44* were all significantly increased, whereas the level of *Erbb2* was unchanged, and the level of *Erbb4* was reduced in the sciatic nerves of P14 *P0CreHgs*^{fl} mice compared with controls (Fig. 9*A*), indicating that Schwann cell loss of HGS disrupts the regulation of components of the ERBB signaling pathway.

Because the ERBB2/3 receptors play an essential role in Schwann cell development and myelination (Riethmacher et al., 1997; Garratt et al., 2000; Brinkmann et al., 2008); we examined whether loss of HGS altered either the levels or activation of proteins in the ERBB pathway. The activation of the ERBB2/3 receptors by NRG1 results in their autophosphorylation, which can be measured using phosphospecific ERBB2/3 Abs. Although there was no difference in the total levels of ERBB2 within the first 2 weeks of postnatal development (Fig. 9*B*,*C*), the levels of phosphorylated ERBB2 were significantly elevated in *P0CreHgs*^{fl} mice compared with controls at both P7 and P14 (Fig. 9*B*,*D*). In contrast, we observed a significant increase in the levels of total ERBB3 in the sciatic nerve extracts of the *P0CreHgs*^{fl} mice at P14, but not at P7, when compared with controls (Fig. 9*E*,*F*). Although we observed an increase in the levels of pERBB3 in the sciatic nerves of the P14 *P0CreHgs*^{fl} mice, this difference was not significant when normalized against the total ERBB3 levels detected in the mice (Fig. 9*G*). These results are consistent with the transcriptome and qPCR results of increased levels of *Erbb3* mRNA without a corresponding change in *Erbb2* mRNA in the sciatic nerves of P14 *P0CreHgs*^{fl} mice. Together, these data suggest that loss of HGS altered the expression of components of the ERBB pathway and the activation of the ERBB2 receptor in Schwann cells.

Loss of HGS impairs AKT signaling

The ERBB2/3 receptors activate several intracellular signaling pathways, including the PI3K-AKT kinase and ERK pathways, which are essential for Schwann cell development and myelination (Monje et al., 2006, 2008; Syed et al., 2010; Newbern et al., 2011; Heller et al., 2014; Domenech-Estévez et al., 2016). To determine whether loss of HGS in Schwann cells affects these pathways, we examined the activated state of these kinases using Abs that recognize the phosphorylated forms of AKT and ERK. As AKT is phosphorylated at T308 by PDK1 and at S473 by mTORC2, these experiments examined the phosphorylated state of AKT at both of these positions. We found that pAKT (T308) was significantly reduced in sciatic nerve extracts from P14 *P0CreHgs*^{fl} mice compared with controls (Fig. 9*H*,*I*). In contrast,

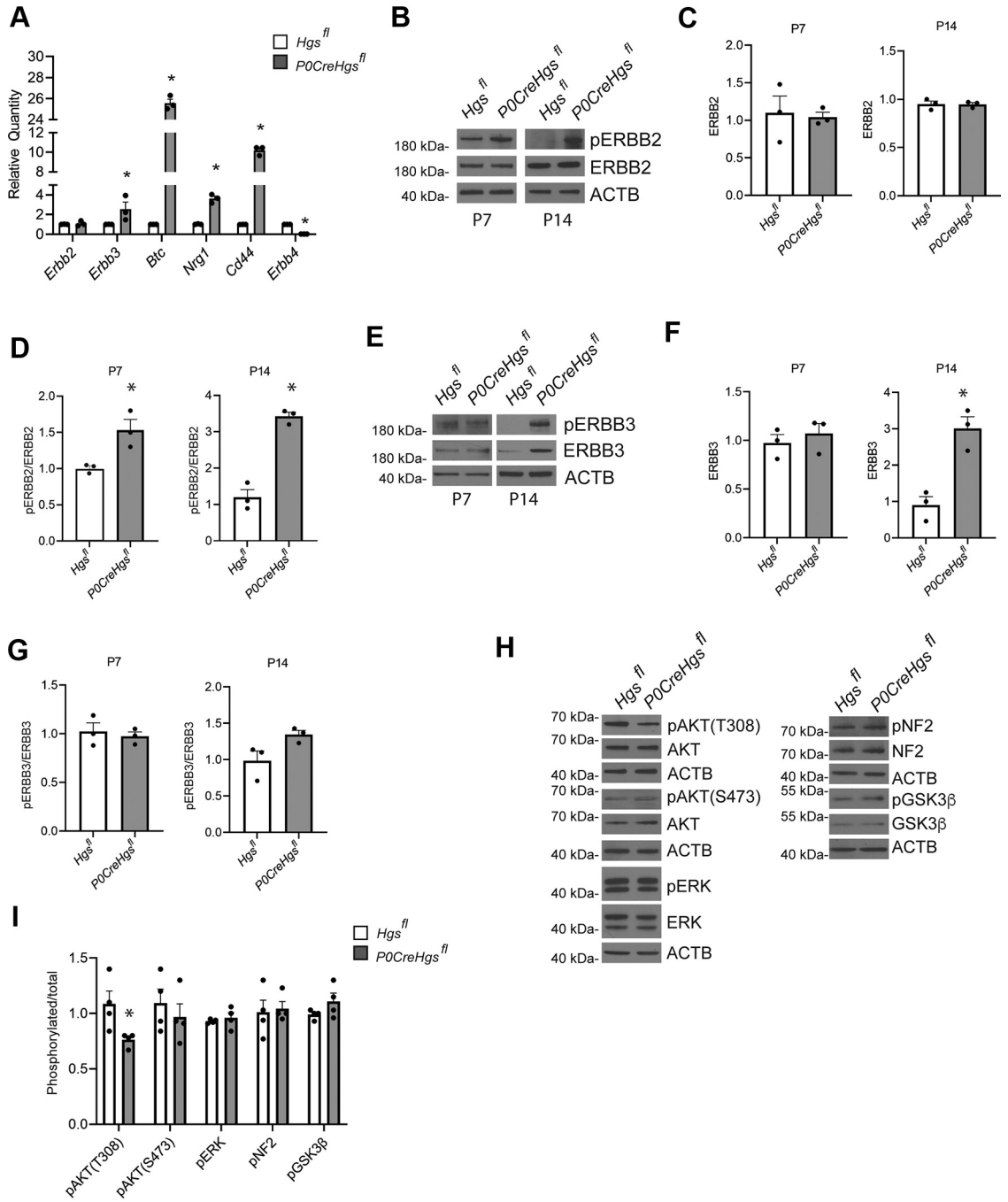

Figure 9. Altered expression of the ERBB2/3 pathway in sciatic nerves of HGS-deficient mice. (***A***) Quantitation of mRNA levels of components in the ERBB pathway in sciatic nerves of P14 *P0CreHgs*^{fl} and *Hgs*^{fl} mice (*Erbb2* p= 0.51, *Erbb3* $p = 8.0 \times 10^{-4}$, *Btc* $p = 1.0 \times 10^{-15}$, *Nrg1* $p = 5.14 \times 10^{-10}$, *Cd44* $p = 1.0 \times 10^{-15}$, *Erbb4* $p = 1.0 \times 10^{-13}$). Data are shown as mean ± SEM and are plotted relative to levels found in *Hgs*^{fl} control mice, $n = 3$ mice per genotype. Student's t test was used to determine whether there was a significant difference in the means of the datasets. ***B–D***, Representative immunoblots (***B***), (***C***) quantitation of ERBB2 (P7 $p = 0.71$, P14 $p = 0.14$), and (***D***) pERBB2 normalized to total ERBB2 (P7 $p = 0.0127$, P14 $p =$ 0.00,741). ***E–G***, Representative immunoblots (***E***), (***F***) quantitation of ERBB3 (P7 $p = 0.34$, P14 $p = 0.0034$), and (***G***) pERBB3 normalized to total ERBB3 (P7 $p = 0.647$, P14 $p = 0.0736$) in sciatic nerve extracts of *Hgs*^{fl} and *P0CreHgs*^{fl} mice. ACTB was used as a loading control. Data are shown as mean ± SEM, $n = 3$ mice per genotype. ***H***, Representative immunoblots of the levels of pAKT(T308), pAKT(S473), AKT, pERK, ERK, pNF2 NF2, pGSK3β and GSK3β. ***I***, Quantitation of pAKT(T308) ($p = 0.038$), pAKT(S473) ($p = 0.74$), pERK ($p = 0.55$), pNF2 ($p = 0.7925$) and pGSK3β ($p = 0.1467$) levels in sciatic nerve extracts from P14 *Hgs*^{fl} and *P0CreHgs*^{fl} mice. ACTB was used as a loading control. Data are shown as mean ± SEM, $n = 4$ mice per genotype. Student's t test was used to determine whether there was a significant difference in the means of the datasets. * indicates $p < 0.05$.

no significant differences were observed in pAKT (S473), pERK, or pGSK3β expression in the sciatic nerves from P14 *P0CreHgs*^{fl} mice and controls (Fig. 9*H*,*I*). Although HGS has also been shown to interact with NF2 and regulate its signaling (Gutmann et al., 2001; Sun et al., 2002), when we examined the effect of Schwann-cell-specific loss of HGS on NF2, there was no significant difference in the levels of either total or activated NF2 proteins in the sciatic nerves of the P14 *P0CreHgs*^{fl} mice compared with controls (Fig. 9*H*,*I*).

Discussion

The identification of endosomal genes linked to demyelinating forms of CMT motivated our interest to understand the role of

the endocytic pathway during myelination. In this study, we used a targeted Schwann-cell-specific deletion of HGS to disrupt the endosomal sorting pathway in Schwann cells and examine its effect on peripheral nerve myelination. We found that loss of HGS delayed the transition of promyelinating Schwann cells to myelinating Schwann cells and resulted in hypomyelination and aberrant myelination of sciatic nerves, demonstrating that endosomal sorting is required for the normal development of myelinating Schwann cells. Loss of HGS also resulted in increased levels of phosphorylated ERBB2 receptors, increased levels of total ERBB3, and a reduction in the steady-state levels of pAKT (T308), which reinforces the idea that the ESCRT pathway regulates the sorting of the ERBB2/3 receptors and supports a growing body of evidence that ERBB2/3 signaling is disrupted in some demyelinating forms of CMT (Lee et al., 2017).

HGS is expressed in multiple cell types within the nervous system, including neurons and Schwann cells. In our previous report (Watson et al., 2015), we showed that a point mutation in the cargo-binding domain of HGS resulted in thicker myelin sheaths in the sciatic nerves of *teetering* mice. This phenotype differs from the hypomyelination defects that occur when HGS is deleted specifically within Schwann cells. However, as the *teetering* mutation also has dominant effects on both tactile sensitivity and exercise-induced ataxia (Meier, 1967; Watson et al., 2015), it is likely that the differences in myelination between the two mouse models are because of a loss of function of HGS in the *P0CreHgs*^{fl} mice, as opposed to a gain of function in the *teetering* mice, as well as the fact that the *teetering* mutation is expressed in both neurons and Schwann cells.

The development of myelinating Schwann cells requires both extrinsic and intrinsic cellular signals (Jessen and Mirsky, 2008). These signals control the expression of both positive and negative regulators of myelination and ultimately determine the onset and extent of myelination. In the *P0CreHgs*^{fl} mice, loss of HGS disrupted the maturation of myelinating Schwann cells, presumably by preventing the repression of multiple negative regulators of myelination, such as *Sox-2*, *c-Jun*, and *Pax3*, and/or preventing the induction of *Egr2*, a transcriptional factor required for myelination (Topilko et al., 1994; Decker et al., 2006). Similar to what we observed in the HGS-deficient Schwann cells, overexpression of *Sox-2* in Schwann cells inhibited the induction of myelin proteins, increased cell proliferation, and caused severe hypomyelination (Roberts et al., 2017). These findings suggest that endosomal sorting regulates essential cell signaling events that are required for the induction of myelination.

Neuregulin 1 signaling through the ERBB2/3 receptors is critical for many aspects of Schwann cell development, including cell proliferation, migration along peripheral axons, and the induction of myelination (Newbern and Birchmeier, 2010; Salzer, 2015). As deficits in the ERBB2/3 signaling pathway are thought to contribute to peripheral neuropathies, these receptors are seen as potential therapeutic targets for the treatment of CMT (Massa et al., 2006; Fledrich et al., 2014; Lee et al., 2017). A report demonstrated that HGS interacts with ERBB3 (Fosdahl et al., 2017), suggesting that the ERBB3 receptor is a substrate for the ESCRT pathway in Schwann cells. Our finding that loss of HGS increased ERBB3 levels without altering the steady-state level of ERBB2 adds further support to the idea that HGS specifically traffics the ERBB3 receptor through the endolysosomal pathway. As the ERBB2/3 receptors are thought to be internalized and trafficked as a heterodimer to the endosome (Sorkin and Goh, 2009; Bertelsen and Stang, 2014), our data support the idea that these receptors may dissociate and be sorted independently on the endosome (Lenferink et al., 1998).

Although greater levels of phosphorylated ERBB2 is indicative of increased activation of these receptors and is associated with enhanced ERBB signaling, we did not observe any increases in phosphorylated AKT or ERK that would suggest activation of these downstream signaling pathways in the sciatic nerves of the *P0CreHgs*^{fl} mice. Instead, we detected decreased levels of pAKT(T308) in HGS-deficient sciatic nerves. A decrease in pAKT(T308) levels was also observed in the sciatic nerves of mice with a deletion of Tuberous Sclerosis Complex Subunit 1 in Schwann cells that caused hyperactivation of the mTOR pathway during development (Figlia et al., 2017), suggesting the presence of an inhibitory feedback loop that regulates the PI3K pathway. It is possible that the increased activation of pERBB2 in the *P0CreHgs*^{fl} mice may therefore have activated an inhibitory feedback loop leading to a reduction in pAKT(308) (Figlia et al., 2018). Alternatively, AKT can be activated on the endosome (Palfy et al., 2012; Ebner et al., 2017; Sugiyama et al., 2019); it is possible that impaired trafficking of the ERBB2/3 receptors in *P0CreHgs*^{fl} mice disrupted this signaling pathway in Schwann cells. In a similar manner, HGS is required for the activation of signaling pathways downstream of the bone morphogenic receptor by acting as a scaffold to recruit TAK1 and SMAD1/5/8 signaling complexes to the endosome (Miura and Mishina, 2011).

We observed an increased number of myelin outfoldings in the sciatic nerves of HGS-deficient mice at both P28 and 6 months of age, and this finding suggests that HGS is required for the proper formation and maintenance of myelin sheaths. Myelin outfoldings are characteristic of CMT4B1 and CMT4B2, both of which are severe demyelinating neuropathies (Azzedine et al., 2003; Bolino et al., 2004; Bolis et al., 2005; Delague et al., 2007; Robinson et al., 2008; Horn et al., 2012) caused by mutations in the Myotubularin-related protein 2 (MTMR2) and 13 (MTMR13), respectively. MTMRs catalyze the dephosphorylation of phospholipids (Bolis et al., 2007), which are docking sites for the recruitment of signaling molecules to internal membranes. HGS possesses a FYVE domain, which binds PI (3)P and is necessary for its association with the endosome (Komada and Soriano, 1999). It is interesting to note that like our HGS-deficient Schwann cells, loss of MTMR2 leads to myelin outfoldings and increased levels of pERBB2 (Bolino et al., 2004, 2016). Downregulation of NRG1 signaling in *Mtmr2* knock-out Schwann cells rescues the myelin outfoldings, suggesting that deficits in phospholipid signaling can result in localized changes in ERBB signaling and focal enhancement in myelination (Bolino et al., 2016). We speculate that in a similar manner, loss of HGS disrupts the sorting of ERBB receptors, leading to enhanced focal myelination and the production of myelin outfoldings. Future studies will examine whether these outfoldings are localized to the paranodal regions of *P0CreHgs*^{fl} mice, as is observed in the MTMR2-deficient mice.

As a master regulator of endosomal sorting (Kobayashi et al., 2005; Komada and Kitamura, 2005), the requirements of HGS during peripheral nerve myelination are likely to extend beyond those of just the ERBB2/3 receptors. However, the studies detailed in this article provide evidence for the requirement of endosomal sorting of the ERBB2/3 receptors during peripheral nerve myelination and offer possible new targets for therapeutic intervention in the treatment of peripheral neuropathies.

References

Adams L, Carlson BM, Henderson L, Goldman D (1995) Adaptation of nicotinic acetylcholine receptor, myogenin, and MRF4 gene expression to long-term muscle denervation. J Cell Biol 131:1341–1349.

Alvarez-Prats A, Bjelobaba I, Aldworth Z, Baba T, Abebe D, Kim YJ, Stojilkovic SS, Stopfer M, Balla T (2018) Schwann-cell-specific deletion of phosphatidylinositol 4-kinase alpha causes aberrant myelination. Cell Rep 23:2881–2890.

Anders S, Pyl PT, Huber W (2015) HTSeq—a Python framework to work with high-throughput sequencing data. Bioinformatics 31:166–169.

Ang ET, Schäfer R, Baltensperger R, Wernig A, Celio M, Oliver SS (2010) Motor axonal sprouting and neuromuscular junction loss in an animal model of Charcot-Marie-Tooth disease. J Neuropathol Exp Neurol 69:281–293.

Arroyo EJ, Bermingham JR Jr., Rosenfeld MG, Scherer SS (1998) Promyelinating Schwann cells express Tst-1/SCIP/Oct-6. J Neurosci 18:7891–7902.

Azzedine H, Bolino A, Taieb T, Birouk N, Di Duca M, Bouhouche A, Benamou S, Mrabet A, Hammadouche T, Chkili T, Gouider R, Ravazzolo R, Brice A, Laporte J, LeGuern E (2003) Mutations in MTMR13, a new pseudophosphatase homologue of MTMR2 and Sbf1, in two families with an autosomal recessive demyelinating form of Charcot-Marie-Tooth disease associated with early-onset glaucoma. Am J Hum Genet 72:1141–1153.

Barisic N, Claeys KG, Sirotković-Skerlev M, Löfgren A, Nelis E, De Jonghe P, Timmerman V (2008) Charcot-Marie-Tooth disease: a clinico-genetic confrontation. Ann Hum Genet 72:416–441.

Bean AJ, Davanger S, Chou MF, Gerhardt B, Tsujimoto S, Chang Y (2000) Hrs-2 regulates receptor-mediated endocytosis via interactions with Eps15. J Biol Chem 275:15271–15278.

Beirowski B, Babetto E, Golden JP, Chen YJ, Yang K, Gross RW, Patti GJ, Milbrandt J (2014) Metabolic regulator LKB1 is crucial for Schwann cell-mediated axon maintenance. Nat Neurosci 17:1351–1361.

Belleudi F, Leone L, Maggio M, Torrisi MR (2009) Hrs regulates the endocytic sorting of the fibroblast growth factor receptor 2b. Exp Cell Res 315:2181–2191.

Bertelsen V, Stang E (2014) The mysterious ways of ErbB2/HER2 trafficking. Membranes (Basel) 4:424–446.

Berti C, Bartesaghi L, Ghidinelli M, Zambroni D, Figlia G, Chen ZL, Quattrini A, Wrabetz L, Feltri ML (2011) Non-redundant function of dystroglycan and β1 integrins in radial sorting of axons. Development 138:4025–4037.

Bolino A, Bolis A, Previtali SC, Dina G, Bussini S, Dati G, Amadio S, Del Carro U, Mruk DD, Feltri ML, Cheng CY, Quattrini A, Wrabetz L (2004) Disruption of Mtmr2 produces CMT4B1-like neuropathy with myelin outfolding and impaired spermatogenesis. J Cell Biol 167:711–721.

Bolino A, Piguet F, Alberizzi V, Pellegatta M, Rivellini C, Guerrero-Valero M, Noseda R, Brombin C, Nonis A, D'Adamo P, Taveggia C, Previtali SC (2016) Niacin-mediated Tace activation ameliorates CMT neuropathies with focal hypermyelination. EMBO Mol Med 8:1438–1454.

Bolis A, Coviello S, Bussini S, Dina G, Pardini C, Previtali SC, Malaguti M, Morana P, Del Carro U, Feltri ML, Quattrini A, Wrabetz L, Bolino A (2005) Loss of Mtmr2 phosphatase in Schwann cells but not in motor neurons causes Charcot-Marie-Tooth type 4B1 neuropathy with myelin outfoldings. J Neurosci 25:8567–8577.

Bolis A, Zordan P, Coviello S, Bolino A (2007) Myotubularin-related (MTMR) phospholipid phosphatase proteins in the peripheral nervous system. Mol Neurobiol 35:308–316.

Brennan KM, Bai Y, Shy ME (2015) Demyelinating CMT—what's known, what's new and what's in store? Neurosci Lett 596:14–26.

Brinkmann BG, Agarwal A, Sereda MW, Garratt AN, Müller T, Wende H, Stassart RM, Nawaz S, Humml C, Velanac V, Radyushkin K, Goebbels S, Fischer TM, Franklin RJ, Lai C, Ehrenreich H, Birchmeier C, Schwab MH, Nave KA (2008) Neuregulin-1/ErbB signaling serves distinct functions in myelination of the peripheral and central nervous system. Neuron 59:581–595.

Brown MJ, Asbury AK (1981) Schwann cell proliferation in the postnatal mouse: timing and topography. Exp Neurol 74:170–186.

Cetin H, Beeson D, Vincent A, Webster R (2020) The structure, function, and physiology of the fetal and adult acetylcholine receptor in muscle. Front Mol Neurosci 13:581097.

Chanut-Delalande H, Jung AC, Baer MM, Lin L, Payre F, Affolter M (2010) The Hrs/Stam complex acts as a positive and negative regulator of RTK signaling during *Drosophila* development. PLoS One 5:e10245.

Chow CY, Zhang Y, Dowling JJ, Jin N, Adamska M, Shiga K, Szigeti K, Shy ME, Li J, Zhang X, Lupski JR, Weisman LS, Meisler MH (2007) Mutation of FIG4 causes neurodegeneration in the pale tremor mouse and patients with CMT4J. Nature 448:68–72.

Cipriani S, Phan V, Medard JJ, Horvath R, Lochmuller H, Chrast R, Roos A, Spendiff S (2018) Neuromuscular junction changes in a mouse model of Charcot-Marie-Tooth disease type 4C. Int J Mol Sci 19:4072.

Colby J, Nicholson R, Dickson KM, Orfali W, Naef R, Suter U, Snipes GJ (2000) PMP22 carrying the trembler or trembler-J mutation is intracellularly retained in myelinating Schwann cells. Neurobiol Dis 7:561–573.

Cullen PJ, Steinberg F (2018) To degrade or not to degrade: mechanisms and significance of endocytic recycling. Nat Rev Mol Cell Biol 19:679–696.

Dauner K, Eid W, Raghupathy R, Presley JF, Zha X (2017) mTOR complex 1 activity is required to maintain the canonical endocytic recycling pathway against lysosomal delivery. J Biol Chem 292:5737–5747.

Decker L, Desmarquet-Trin-Dinh C, Taillebourg E, Ghislain J, Vallat JM, Charnay P (2006) Peripheral myelin maintenance is a dynamic process requiring constant Krox20 expression. J Neurosci 26:9771–9779.

Delague V, Jacquier A, Hamadouche T, Poitelon Y, Baudot C, Boccaccio I, Chouery E, Chaouch M, Kassouri N, Jabbour R, Grid D, Megarbane A, Haase G, Lévy N (2007) Mutations in FGD4 encoding the Rho GDP/GTP exchange factor FRABIN cause autosomal recessive Charcot-Marie-Tooth type 4H. Am J Hum Genet 81:1–16.

Dobin A, Davis CA, Schlesinger F, Drenkow J, Zaleski C, Jha S, Batut P, Chaisson M, Gingeras TR (2013) STAR: ultrafast universal RNA-seq aligner. Bioinformatics 29:15–21.

Domenech-Estévez E, Baloui H, Meng X, Zhang Y, Deinhardt K, Dupree JL, Einheber S, Chrast R, Salzer JL (2016) Akt regulates axon wrapping and myelin sheath thickness in the PNS. J Neurosci 36:4506–4521.

Dong C, Palladino SP, Helton ES, Ubogu EE (2016) The pathogenic relevance of alphaM-integrin in Guillain-Barré syndrome. Acta Neuropathol 132:739–752.

Dong C, Greathouse KM, Beacham RL, Palladino SP, Helton ES, Ubogu EE (2017) Fibronectin connecting segment-1 peptide inhibits pathogenic leukocyte trafficking and inflammatory demyelination in experimental models of chronic inflammatory demyelinating polyradiculoneuropathy. Exp Neurol 292:35–45.

Ebner M, Lučić I, Leonard TA, Yudushkin I (2017) PI(3,4,5)P3 engagement restricts Akt activity to cellular membranes. Mol Cell 65:416–431.

Eiber N, Rehman M, Kravic B, Rudolf R, Sandri M, Hashemolhosseini S (2019) Loss of protein kinase Csnk2b/CK2β at neuromuscular junctions affects morphology and dynamics of aggregated nicotinic acetylcholine receptors, neuromuscular transmission, and synaptic gene expression. Cells 8:940.

Erdem S, Mendell JR, Sahenk Z (1998) Fate of Schwann cells in CMT1A and HNPP: evidence for apoptosis. J Neuropathol Exp Neurol 57:635–642.

Evans S, Goldman D, Heinemann S, Patrick J (1987) Muscle acetylcholine receptor biosynthesis. Regulation by transcript availability. J Biol Chem 262:4911–4916.

Feltri ML, D'Antonio M, Previtali S, Fasolini M, Messing A, Wrabetz L (1999) P0-Cre transgenic mice for inactivation of adhesion molecules in Schwann cells. Ann N Y Acad Sci 883:116–123.

Figlia G, Norrmén C, Pereira JA, Gerber D, Suter U (2017) Dual function of the PI3K-Akt-mTORC1 axis in myelination of the peripheral nervous system. Elife 6:e29241.

Figlia G, Gerber D, Suter U (2018) Myelination and mTOR. Glia 66:693–707.

Fledrich R, Stassart RM, Klink A, Rasch LM, Prukop T, Haag L, Czesnik D, Kungl T, Abdelaal TA, Keric N, Stadelmann C, Brück W, Nave KA, Sereda MW (2014) Soluble neuregulin-1 modulates disease pathogenesis in rodent models of Charcot-Marie-Tooth disease 1A. Nat Med 20:1055–1061.

Fosdahl AM, Dietrich M, Schink KO, Malik MS, Skeie M, Bertelsen V, Stang E (2017) ErbB3 interacts with Hrs and is sorted to lysosomes for degradation. Biochim Biophys Acta Mol Cell Res 1864:2241–2252.

Garratt AN, Voiculescu O, Topilko P, Charnay P, Birchmeier C (2000) A dual role of erbB2 in myelination and in expansion of the schwann cell precursor pool. J Cell Biol 148:1035–1046.

Gerber D, Pereira JA, Gerber J, Tan G, Dimitrieva S, Yángüez E, Suter U (2021) Transcriptional profiling of mouse peripheral nerves to the single-cell level to build a sciatic nerve ATlas (SNAT). Elife 10:e58591.

Goh LK, Sorkin A (2013) Endocytosis of receptor tyrosine kinases. Cold Spring Harb Perspect Biol 5:a017459.

Goldman D, Brenner HR, Heinemann S (1988) Acetylcholine receptor alpha-, beta-, gamma-, and delta-subunit mRNA levels are regulated by muscle activity. Neuron 1:329–333.

Gomez-Sanchez JA, et al. (2015) Schwann cell autophagy, myelinophagy, initiates myelin clearance from injured nerves. J Cell Biol 210:153–168.

Grove M, Kim H, Santerre M, Krupka AJ, Han SB, Zhai J, Cho JY, Park R, Harris M, Kim S, Sawaya BE, Kang SH, Barbe MF, Cho SH, Lemay MA, Son YJ (2017) YAP/TAZ initiate and maintain Schwann cell myelination. Elife 6:e20982.

Gutmann DH, Haipek CA, Burke SP, Sun CX, Scoles DR, Pulst SM (2001) The NF2 interactor, hepatocyte growth factor-regulated tyrosine kinase substrate (HRS), associates with merlin in the "open" conformation and suppresses cell growth and motility. Hum Mol Genet 10:825–834.

Hahn AF, Chang Y, Webster HD (1987) Development of myelinated nerve fibers in the sixth cranial nerve of the rat: a quantitative electron microscope study. J Comp Neurol 260:491–500.

Hanyaloglu AC, McCullagh E, von Zastrow M (2005) Essential role of Hrs in a recycling mechanism mediating functional resensitization of cell signaling. EMBO J 24:2265–2283.

Haugen LH, Skjeldal FM, Bergeland T, Bakke O (2017) Endosomal binding kinetics of Eps15 and Hrs specifically regulate the degradation of RTKs. Sci Rep 7:17962.

Heller BA, Ghidinelli M, Voelkl J, Einheber S, Smith R, Grund E, Morahan G, Chandler D, Kalaydjieva L, Giancotti F, King RH, Fejes-Toth AN, Fejes-Toth G, Feltri ML, Lang F, Salzer JL (2014) Functionally distinct PI 3-kinase pathways regulate myelination in the peripheral nervous system. J Cell Biol 204:1219–1236.

Hislop JN, Marley A, Von Zastrow M (2004) Role of mammalian vacuolar protein-sorting proteins in endocytic trafficking of a non-ubiquitinated G protein-coupled receptor to lysosomes. J Biol Chem 279:22522–22531.

Horn M, Baumann R, Pereira JA, Sidiropoulos PNM, Somandin C, Welzl H, Stendel C, Luhmann T, Wessig C, Toyka KV, Relvas JB, Senderek J, Suter U (2012) Myelin is dependent on the Charcot-Marie-Tooth type 4H disease culprit protein FRABIN/FGD4 in Schwann cells. Brain 135:3567–3583.

Huang SH, Zhao L, Sun ZP, Li XZ, Geng Z, Zhang KD, Chao MV, Chen ZY (2009) Essential role of Hrs in endocytic recycling of full-length TrkB receptor but not its isoform TrkB.T1. J Biol Chem 284:15126–15136.

Huang HR, Chen ZJ, Kunes S, Chang GD, Maniatis T (2010) Endocytic pathway is required for *Drosophila* Toll innate immune signaling. Proc Natl Acad Sci U S A 107:8322–8327.

Hunter M, Bernard R, Freitas E, Boyer A, Morar B, Martins IJ, Tournev I, Jordanova A, Guergelcheva V, Ishpekova B, Kremensky I, Nicholson G, Schlotter B, Lochmüller H, Voit T, Colomer J, Thomas PK, Levy N, Kalaydjieva L (2003) Mutation screening of the N-myc downstream-regulated gene 1 (NDRG1) in patients with Charcot-Marie-Tooth disease. Hum Mutat 22:129–135.

Hurley JH (2008) ESCRT complexes and the biogenesis of multivesicular bodies. Curr Opin Cell Biol 20:4–11.

Hurley JH, Emr SD (2006) The ESCRT complexes: structure and mechanism of a membrane-trafficking network. Annu Rev Biophys Biomol Struct 35:277–298.

Jessen KR, Mirsky R (2005) The origin and development of glial cells in peripheral nerves. Nat Rev Neurosci 6:671–682.

Jessen KR, Mirsky R (2008) Negative regulation of myelination: relevance for development, injury, and demyelinating disease. Glia 56:1552–1565.

Jovic M, Sharma M, Rahajeng J, Caplan S (2010) The early endosome: a busy sorting station for proteins at the crossroads. Histol Histopathol 25:99–112.

Kachhap SK, Faith D, Qian DZ, Shabbeer S, Galloway NL, Pili R, Denmeade SR, DeMarzo AM, Carducci MA (2007) The N-Myc down regulated Gene1 (NDRG1) Is a Rab4a effector involved in vesicular recycling of E-cadherin. PLoS One 2:e844.

Kalaydjieva L, Gresham D, Gooding R, Heather L, Baas F, de Jonge R, Blechschmidt K, Angelicheva D, Chandler D, Worsley P, Rosenthal A, King RH, Thomas PK (2000) N-myc downstream-regulated gene 1 is mutated in hereditary motor and sensory neuropathy-Lom. Am J Hum Genet 67:47–58.

Kobayashi OH, Tanaka N, Sugamura K (2005) Hrs, a mammalian master molecule in vesicular transport and protein-sorting, suppresses the degradation of ESCRT proteins STAM1 and STAM2. Cell Struct Funct 30:75–75.

Komada M, Soriano P (1999) Hrs, a FYVE finger protein localized to early endosomes, is implicated in vesicular traffic and required for ventral folding morphogenesis. Genes Dev 13:1475–1485.

Komada M, Kitamura N (2005) The Hrs/STAM complex in the downregulation of receptor tyrosine kinases. J Biochem 137:1–8.

Kong L, Wang X, Choe DW, Polley M, Burnett BG, Bosch-Marcé M, Griffin JW, Rich MM, Sumner CJ (2009) Impaired synaptic vesicle release and immaturity of neuromuscular junctions in spinal muscular atrophy mice. J Neurosci 29:842–851.

Lee SM, Olzmann JA, Chin LS, Li L (2011) Mutations associated with Charcot-Marie-Tooth disease cause SIMPLE protein mislocalization and degradation by the proteasome and aggresome-autophagy pathways. J Cell Sci 124:3319–3331.

Lee SM, Chin LS, Li L (2012) Charcot-Marie-Tooth disease-linked protein SIMPLE functions with the ESCRT machinery in endosomal trafficking. J Cell Biol 199:799–816.

Lee SM, Chin LS, Li L (2017) Dysregulation of ErbB receptor trafficking and signaling in demyelinating Charcot-Marie-Tooth disease. Mol Neurobiol 54:87–100.

Lenferink AE, Pinkas-Kramarski R, van de Poll ML, van Vugt MJ, Klapper LN, Tzahar E, Waterman H, Sela M, van Zoelen EJ, Yarden Y (1998) Differential endocytic routing of homo- and hetero-dimeric ErbB tyrosine kinases confers signaling superiority to receptor heterodimers. EMBO J 17:3385–3397.

Li W, Zhu H, Zhao X, Brancho D, Liang Y, Zou Y, Bennett C, Chow CW (2015) Dysregulated inflammatory signaling upon Charcot-Marie-Tooth type 1C mutation of SIMPLE protein. Mol Cell Biol 35:2464–2478.

Logan AM, Mammel AE, Robinson DC, Chin AL, Condon AF, Robinson FL (2017) Schwann cell-specific deletion of the endosomal PI 3-kinase Vps34 leads to delayed radial sorting of axons, arrested myelination, and abnormal ErbB2-ErbB3 tyrosine kinase signaling. Glia 65:1452–1470.

Love MI, Huber W, Anders S (2014) Moderated estimation of fold change and dispersion for RNA-seq data with DESeq2. Genome Biol 15:550.

Lupo V, Galindo MI, Martinez-Rubio D, Sevilla T, Vílchez JJ, Palau F, Espinós C (2009) Missense mutations in the SH3TC2 protein causing Charcot-Marie-Tooth disease type 4C affect its localization in the plasma membrane and endocytic pathway. Hum Mol Genet 18:4603–4614.

Massa R, Palumbo C, Cavallaro T, Panico MB, Bei R, Terracciano C, Rizzuto N, Bernardi G, Modesti A (2006) Overexpression of ErbB2 and ErbB3 receptors in Schwann cells of patients with Charcot-Marie-Tooth disease type 1A. Muscle Nerve 33:342–349.

McNally KE, Cullen PJ (2018) Endosomal retrieval of cargo: retromer is not alone. Trends Cell Biol 28:807–822.

Meier H (1967) The neuropathy of teetering, a neurological mutation in the mouse. Arch Neurol 16:59–66.

Miura S, Mishina Y (2011) Hepatocyte growth factor-regulated tyrosine kinase substrate (Hgs) is involved in BMP signaling through phosphorylation of SMADs and TAK1 in early mouse embryo. Dev Dyn 240:2474–2481.

Monje PV, Bunge MB, Wood PM (2006) Cyclic AMP synergistically enhances neuregulin-dependent ERK and Akt activation and cell cycle progression in Schwann cells. Glia 53:649–659.

Monje PV, Athauda G, Wood PM (2008) Protein kinase A-mediated gating of neuregulin-dependent ErbB2-ErbB3 activation underlies the synergistic action of cAMP on Schwann cell proliferation. J Biol Chem 283:34087–34100.

Nandini S, Conley Calderon JL, Sabblah TT, Love R, King LE, King SJ (2019) Mice with an autosomal dominant Charcot-Marie-Tooth type 2O disease mutation in both dynein alleles display severe moto-sensory phenotypes. Sci Rep 9:11979.

Naslavsky N, Caplan S (2018) The enigmatic endosome—sorting the ins and outs of endocytic trafficking. J Cell Sci 131:jcs216499.

Newbern J, Birchmeier C (2010) Nrg1/ErbB signaling networks in Schwann cell development and myelination. Semin Cell Dev Biol 21:922–928.

Newbern JM, Li X, Shoemaker SE, Zhou J, Zhong J, Wu Y, Bonder D, Hollenback S, Coppola G, Geschwind DH, Landreth GE, Snider WD

(2011) Specific functions for ERK/MAPK signaling during PNS development. Neuron 69:91–105.
Orita S, Henry K, Mantuano E, Yamauchi K, De Corato A, Ishikawa T, Feltri ML, Wrabetz L, Gaultier A, Pollack M, Ellisman M, Takahashi K, Gonias SL, Campana WM (2013) Schwann cell LRP1 regulates remak bundle ultrastructure and axonal interactions to prevent neuropathic pain. J Neurosci 33:5590–5602.
Palfy M, Remenyi A, Korcsmaros T (2012) Endosomal crosstalk: meeting points for signaling pathways. Trends Cell Biol 22:447–456.
Pereira JA, Lebrun-Julien F, Suter U (2012) Molecular mechanisms regulating myelination in the peripheral nervous system. Trends Neurosci 35:123–134.
Perkins CS, Aguayo AJ, Bray GM (1981) Schwann cell multiplication in Trembler mice. Neuropathol Appl Neurobiol 7:115–126.
Pietiäinen V, Vassilev B, Blom T, Wang W, Nelson J, Bittman R, Bäck N, Zelcer N, Ikonen E (2013) NDRG1 functions in LDL receptor trafficking by regulating endosomal recycling and degradation. J Cell Sci 126:3961–3971.
Pisciotta C, Shy ME (2018) Neuropathy. Handb Clin Neurol 148:653–665.
Raiborg C, Malerød L, Pedersen NM, Stenmark H (2008) Differential functions of Hrs and ESCRT proteins in endocytic membrane trafficking. Exp Cell Res 314:801–813.
Redpath GMI, Betzler VM, Rossatti P, Rossy J (2020) Membrane heterogeneity controls cellular endocytic trafficking. Front Cell Dev Biol 8:757.
Riethmacher D, Sonnenberg-Riethmacher E, Brinkmann V, Yamaai T, Lewin GR, Birchmeier C (1997) Severe neuropathies in mice with targeted mutations in the ErbB3 receptor. Nature 389:725–730.
Roberts SL, Dun XP, Doddrell RDS, Mindos T, Drake LK, Onaitis MW, Florio F, Quattrini A, Lloyd AC, D'Antonio M, Parkinson DB (2017) Sox2 expression in Schwann cells inhibits myelination *in vivo* and induces influx of macrophages to the nerve. Development 144:3114–3125.
Robinson FL, Niesman IR, Beiswenger KK, Dixon JE (2008) Loss of the inactive myotubularin-related phosphatase Mtmr13 leads to a Charcot-Marie-Tooth 4B2-like peripheral neuropathy in mice. Proc Natl Acad Sci U S A 105:4916–4921.
Rusten TE, Vaccari T, Stenmark H (2011) Shaping development with ESCRTs. Nat Cell Biol 14:38–45.
Salzer JL (2015) Schwann cell myelination. Cold Spring Harb Perspect Biol 7: a020529.
Sancho S, Young P, Suter U (2001) Regulation of Schwann cell proliferation and apoptosis in PMP22-deficient mice and mouse models of Charcot-Marie-Tooth disease type 1A. Brain 124:2177–2187.
Seburn KL, Nangle LA, Cox GA, Schimmel P, Burgess RW (2006) An active dominant mutation of glycyl-tRNA synthetase causes neuropathy in a Charcot-Marie-Tooth 2D mouse model. Neuron 51:715–726.
Sidiropoulos PN, Miehe M, Bock T, Tinelli E, Oertli CI, Kuner R, Meijer D, Wollscheid B, Niemann A, Suter U (2012) Dynamin 2 mutations in Charcot-Marie-Tooth neuropathy highlight the importance of clathrin-mediated endocytosis in myelination. Brain 135:1395–1411.
Sleigh JN, Grice SJ, Burgess RW, Talbot K, Cader MZ (2014) Neuromuscular junction maturation defects precede impaired lower motor neuron connectivity in Charcot-Marie-Tooth type 2D mice. Hum Mol Genet 23:2639–2650.
Sorkin A, Goh LK (2009) Endocytosis and intracellular trafficking of ErbBs. Exp Cell Res 315:683–696.
Spaulding EL, Sleigh JN, Morelli KH, Pinter MJ, Burgess RW, Seburn KL (2016) Synaptic deficits at neuromuscular junctions in two mouse models of Charcot-Marie-Tooth type 2d. J Neurosci 36:3254–3267.
Street VA, Bennett CL, Goldy JD, Shirk AJ, Kleopa KA, Tempel BL, Lipe HP, Scherer SS, Bird TD, Chance PF (2003) Mutation of a putative protein degradation gene LITAF/SIMPLE in Charcot-Marie-Tooth disease 1C. Neurology 60:22–26.
Sugiyama MG, Fairn GD, Antonescu CN (2019) Akt-ing up just about everywhere: compartment-specific akt activation and function in receptor tyrosine kinase signaling. Front Cell Dev Biol 7:70.
Sun CX, Haipek C, Scoles DR, Pulst SM, Giovannini M, Komada M, Gutmann DH (2002) Functional analysis of the relationship between the neurofibromatosis 2 tumor suppressor and its binding partner, hepatocyte growth factor-regulated tyrosine kinase substrate. Hum Mol Genet 11:3167–3178.
Syed N, Reddy K, Yang DP, Taveggia C, Salzer JL, Maurel P, Kim HA (2010) Soluble neuregulin-1 has bifunctional, concentration-dependent effects on Schwann cell myelination. J Neurosci 30:6122–6131.
Topilko P, Schneider-Maunoury S, Levi G, Baron-Van Evercooren A, Chennoufi AB, Seitanidou T, Babinet C, Charnay P (1994) Krox-20 controls myelination in the peripheral nervous system. Nature 371:796–799.
Ubogu EE, Yosef N, Xia RH, Sheikh KA (2012) Behavioral, electrophysiological, and histopathological characterization of a severe murine chronic demyelinating polyneuritis model. J Peripher Nerv Syst 17:53–61.
Vaden JH, Bhattacharyya BJ, Chen PC, Watson JA, Marshall AG, Phillips SE, Wilson JA, King GD, Miller RJ, Wilson SM (2015) Ubiquitin-specific protease 14 regulates c-Jun N-terminal kinase signaling at the neuromuscular junction. Mol Neurodegener 10:3.
Villaseñor R, Kalaidzidis Y, Zerial M (2016) Signal processing by the endosomal system. Curr Opin Cell Biol 39:53–60.
Watson JA, Bhattacharyya BJ, Vaden JH, Wilson JA, Icyuz M, Howard AD, Phillips E, DeSilva TM, Siegal GP, Bean AJ, King GD, Phillips SE, Miller RJ, Wilson SM (2015) Motor and sensory deficits in the teetering mice result from mutation of the ESCRT component HGS. PLoS Genet 11: e1005290.
Witzemann V (1989) Control of acetylcholine receptors in skeletal muscle. J Protein Chem 8:333–335.
Yan Q, Sun W, Kujala P, Lotfi Y, Vida TA, Bean AJ (2005) CART: an Hrs/actinin-4/BERP/myosin V protein complex required for efficient receptor recycling. Mol Biol Cell 16:2470–2482.
Yin X, Kidd GJ, Pioro EP, McDonough J, Dutta R, Feltri ML, Wrabetz L, Messing A, Wyatt RM, Balice-Gordon RJ, Trapp BD (2004) Dysmyelinated lower motor neurons retract and regenerate dysfunctional synaptic terminals. J Neurosci 24:3890–3898.
Zoidl G, Blass-Kampmann S, D'Urso D, Schmalenbach C, Müller HW (1995) Retroviral-mediated gene transfer of the peripheral myelin protein PMP22 in Schwann cells: modulation of cell growth. EMBO J 14:1122–1128.